JM PAPERS

Reynolds number dependence of azimuthal and streamwise pipe flow structures

E.-S. Zanoun[1],†, Y. Dewidar[1] and C. Egbers[1]

[1]Department of Aerodynamics and Fluid Mechanics, BTU Cottbus-Senftenberg, D-03046 Cottbus, Germany

This paper revisits the study by Bailey *et al.* (*J. Fluid Mech.*, vol. 615, 2008, pp. 121–138), adopting a higher-fidelity calibration approach to reveal subtle flow variations with Reynolds numbers that were not discernible previously. The paper aims therefore to provide insights into the characteristics of azimuthal and streamwise pipe flow structures adopting two-point joint statistics and spectral analysis for shear Reynolds numbers in the range $2 \times 10^3 \leq Re_\tau \leq 16 \times 10^3$, where Re_τ is based on the wall friction velocity u_τ, the pipe radius R, and the fluid kinematic viscosity ν. The streamwise velocity fluctuations were measured at four wall-normal locations, $0.1 \leq x_2/R \leq 0.7$, covering the logarithmic and core regions of fully developed turbulent pipe flow based on 35–41 azimuthal probe separations using, simultaneously, two single hot-wire probes. A unique *in situ* calibration approach for both probes was adopted where a potential flow was insured, resulting in consistent and precise pipe flow data. The azimuthal velocity correlation, the cross-power spectral density and the coherence function of the streamwise velocity fluctuations are discussed, revealing a clear dependence of the azimuthal scales of the large and very large flow motions on the wall-normal location, the azimuthal separation, the streamwise wavenumber and the Reynolds number. Along the logarithmic region, a linear growth of the azimuthal scales of the large- and very-large-scale structures was observed; however, they do scale nonlinearly and reach their maximum sizes in the core region, i.e. near the centreline of the pipe. Additionally, the streamwise very-large- and large-scale motions were evaluated using the premultiplied energy spectra, showing wavelengths $\approx 18R$ and $\approx 3R$ for $Re_\tau \approx 16 \times 10^3$ at half of the pipe radius, respectively.

Key words: pipe flow

† Email address for correspondence: elsayed.zanoun@aol.com

1. Introduction and aim of the work

Over decades and still continuing, the two-point velocity–velocity and velocity–pressure gradient correlation experiments are of fundamental importance in theories of turbulence and understanding dynamics of wall-bounded (i.e. boundary layer, pipe and plane channel) shear flows; see e.g. Townsend (1956), Monin & Yaglom (1971), Cantwell (1981), Oberlack & Peters (1993), Jovanović, Ye & Durst (1995), Jovanović (2004), Wallace (2014) and Chen (2019). Among the three classes of wall-bounded shear flows, an increasing interest addressing pipe flow structures requires velocity and pressure data with high enough spatial and temporal resolutions using optical, thermal and pressure probes; e.g. Hellström *et al.* (2011) and Monty *et al.* (2007). The correlations, probability density functions and power spectra of such velocity and pressure signals represent vital statistical tools to analyse the structure of the organized motions of turbulent pipe flow data. The nature of such organized motions – in particular, their spatial details and dynamical significance – was addressed in various papers; see e.g. Theodorsen (1952), Townsend (1956), Lumley (1967), Sabot, Renault & Comte-Bellot (1973), Cantwell (1981), Hussain (1983, 1986), Robinson (1991), Wark & Nagib (1991), Tomkins & Adrian (2003), Monty *et al.* (2007), Bailey *et al.* (2008), Bailey & Smits (2010), Smits, McKeon & Marusic (2011*a*) and Chung *et al.* (2015). Nevertheless, a concrete definition of the origin, nature and time evolution of the coherent structures is still under debate (see e.g. Marusic *et al.* 2010; Jiménez 2018), motivating further investigations to properly characterize the large-scale coherent motions, in particular at high Reynolds numbers.

The early work to isolate the coherent features of the large-scale motions in turbulent boundary layer flows using the temporal correlation of the streamwise velocity component goes back to Townsend (1956) and Grant (1958). Townsend (1956) defined the large-scale motions as energetic structures that are characterized by a long tail on the temporal correlation of the streamwise velocity fluctuations, implying correspondingly long structures in the streamwise direction in the buffer layer where low-speed streaks are revealed, as well as throughout the logarithmic layer and the core/wake region.

Using spatio-temporal correlation, further studies have been carried out – see Hussain (1983), Blackwelder (1988), Fiedler (1988), Robinson (1991) and Holmes *et al.* (1996) – providing further definitions for such large-scale organized motions. Robinson (1991, p. 602), for instance, defined the organized flow structures as 'a three-dimensional region of the flow over which at least one fundamental flow variable (velocity, pressure, temperature, etc.) exhibits significant correlation with itself or with another variable over a range of space and/or time that is significantly larger than the smallest local scales of the flow', motivating studies of turbulent pipe flow structures using two-point velocity correlations; e.g. Monty *et al.* (2007), Bailey *et al.* (2008), Baidya *et al.* (2019) and Han *et al.* (2019).

Monty *et al.* (2007) investigated the azimuthal scales of the large-scale motions in pipe flow through the two-point velocity correlations measured, utilizing a rake of hot-wire probes fixed at the top of the logarithmic region. They claimed that the azimuthal structures in pipe flow were nearly identical to those determined from similar measurements in plane channel and boundary layer flows. However, due to the geometrical considerations of a pipe when compared with either plane channel and/or flat-plate boundary layer flows, its flow structure might be different; see Holmes *et al.* (1997), Kim & Adrian (1999), Marusic *et al.* (2010) and Chung *et al.* (2015). Chung *et al.* (2015) provided a good explanation for the geometrical consideration effects, revealing subtle differences between the boundary layer and the pipe flow in terms of the structure functions for the

streamwise turbulence intensity profile at high Reynolds numbers versus the wall distance, in particular in the logarithmic layer. Marusic *et al.* (2010) attributed also the quantitative differences between the two classes of flows to the interaction with the opposite wall in internal flows, i.e. pipe and channel, and to the intermittency of the outer region in boundary layers, but concluded that it remains a matter of speculation. Therefore, the finding of Monty *et al.* (2007) cannot be generalized since it was based on a single fixed wall-normal position, motivating Bailey *et al.* (2008) to further study changes in the azimuthal scales of the pipe flow.

The objective of the Bailey *et al.* (2008) study was to investigate the wall-normal dependence of the azimuthal scales of the large-scale and very-large-scale structures within the wall-normal distances $0.1 \leq x_2/R \leq 0.5$ for a large range of Reynolds number $7.6 \times 10^4 \leq Re_b \leq 8.3 \times 10^6$ based on the pipe diameter. The experiments by Bailey *et al.* (2008) were conducted with two single hot-wire probes calibrated where the pipe flow was assured to be fully developed turbulent. They calibrated both hot-wire probes using a Pitot probe fixed at the pipe centreline, while the two probes were positioned offset from the pipe centreline, yielding second-order statistics within 10 % uncertainty. The uncertainty level would be even higher if the hot-wire probes were moved towards the vicinity of the pipe wall where the turbulence level is higher, in particular at large Reynolds number. The high uncertainty level in the calibration equations of both hot-wire probes utilized weakened their dynamic responses to small velocity fluctuations that would give rise to substantial levels of deviation in the conclusions drawn (Talluru, Kulandaivelu & Hutchins 2014; Boufidi, Lavagnoli & Fontaneto 2020). This could result, for instance, in an improper effect of the Reynolds number on scaling the azimuthal large-scale structures.

Measurement uncertainty is thus of importance for evaluating turbulence statistics and their dependence on the Reynolds number; see Appendix A. Therefore, we adopted a unique *in situ* calibration approach that provided calibration equations for hot-wire probes with least-squares error better than ± 1 %, resulting in very accurate experimental pipe data. Our main objective is to study, precisely, the effect of wider wall-normal distances $0.1 \leq x_2/R \leq 0.7$ and azimuthal space separations $10° \leq \Delta\theta \leq 210°$ on the velocity correlation $R_{u_1 u_1}(\Delta s, t)$, the cross-power spectral density $G(\Delta s, k_{x_1})$ and the coherence function $\gamma(\Delta s, k_{x_1})$, and consequently on pipe flow azimuthal scales of the large- and very-large-scale structures over the relatively large Reynolds number range $2 \times 10^3 \leq Re_\tau \leq 16 \times 10^3$.

Two-point joint statistics were adopted to investigate the effects of the various parameters discussed earlier and the effect of scale averaging on the azimuthal scales of the large-scale flow motions. The two-point spatial correlation of the streamwise velocity fluctuations $R_{u_1 u_1}(\Delta s, t)$ is therefore of fundamental interest in the present study for the statistical analysis of the azimuthal pipe flow data. It is defined for two locations at the same time instant t as

$$R_{u_1 u_1}(s + \Delta s, t) = \frac{\langle u_1(s, t) \, u_1(s + \Delta s, t) \rangle}{\sqrt{\langle u_1^2(s, t) \rangle} \sqrt{\langle u_1^2(s + \Delta s, t) \rangle}}, \quad (1.1)$$

where $\langle \cdot \rangle$ denotes an ensemble average of velocity fluctuating signals, Δs is the azimuthal space separation, and $u_1(s, t)$ is the streamwise velocity fluctuation as a function of space (s) and time (t). The use of the two-point velocity correlations $R_{u_1 u_1}(s + \Delta s, t)$ to address the azimuthal structures of turbulence in pipe flow requires either using an optical measuring technique such as particle image velocimetry and/or multiple thermal hot-wire probes. The multiple hot-wire probes separated in space are in common use to

U_b (m s^{-1})	Re_b	u_τ (m s^{-1})	Re_τ	ℓ^+	ℓ_c (μm)	T (s)	S_s
7.92	9.81×10^4	0.345	2.3×10^3	29	42	60	1.8×10^6
14.36	17.95×10^4	0.61	4.1×10^3	52	23	60	1.8×10^6
30.76	3.85×10^5	1.21	7.7×10^3	97	13	120	3.6×10^6
47.30	5.59×10^5	1.81	1.15×10^4	145	8	120	3.6×10^6
62.85	7.71×10^5	2.51	1.53×10^4	192	6	120	3.6×10^6

Table 1. Summary of the present main experimental parameters: U_b is the bulk velocity, Re_b is the bulk Reynolds number, u_τ is the wall friction velocity, Re_τ is the shear Reynolds number, $\ell^+ = \ell u_\tau / \nu$ is the hot-wire length in wall units, ℓ_c is the viscous length scale, T is the sampling time, and S_s is the sampling size.

characterize the coherence structures in wall-bounded shear flows as reported earlier (see e.g. Monty *et al.* 2007; Bailey *et al.* 2008), providing highly temporal-resolved velocity data. However, when the near-wall motions are targeted, the length ℓ of the sensing element of the hot-wire probe (see table 1) is an important issue to be considered, in particular at high Reynolds numbers; see Blackwelder & Haritonidis (1983), Ligrani & Bradshaw (1987), Wei & Willmarth (1989) and Gad-el-Hak & Bandyopadhyay (1994). At high Reynolds numbers, the turbulence viscous length scale $\ell_c = \nu/u_\tau$ is much smaller than probe size. The measured velocity signals are thus attenuated, and consequently the small-scale turbulence is not well resolved because of the averaging process. Blackwelder & Haritonidis (1983) suggested sensors having a spatial scale that is less than twenty viscous length scales to provide experimental data free from spatial averaging effects. This physical constraint, combined with the requirement for a hot-wire length-to-diameter ratio $\ell/d \approx 250$, limited turbulence–structure experiments using commercial hot-wire probes at high Reynolds numbers. To account for such inadequate spatial and temporal resolutions of hot-wire probes, correction techniques for the streamwise velocity fluctuations proposed by Hutchins *et al.* (2009), Smits *et al.* (2011*b*) and Hutchins, Monty & Hultmark (2015) for a wide range of the Reynolds number and wire lengths were adopted with success in the present study. Table 1 summarizes the relevant parameters from experiments performed and presented in the paper. The main sections of this paper are summarized as follows. Section 1 highlighted briefly the state of the art of the velocity correlation in wall-bounded flows, in particular in pipe flow. The experimental facility and the hot-wire module are presented in § 2. Section 3 presents the resultant data over a relatively wide range of Reynolds numbers. Section 4 summarizes the outcome of the present study with some concluding remarks. Appendices A and B are presented at the end of the paper. Overall, this paper is intended to provide a good insight into the characteristics of azimuthal and streamwise pipe flow structures, using two-point velocity correlations and spectral analysis.

2. Experimental set-up and hot-wire calibration

2.1. *The pipe facility*

Experiments were carried out utilizing the large pipe facility (CoLaPipe) located at Brandenburg University of Technology Cottbus–Senftenberg. The CoLaPipe (figure 1*a*) is a closed-return facility equipped with a water cooler to keep the air temperature constant inside the pipe test section. The facility allows measurements for shear Reynolds number Re_τ in the range $8 \times 10^2 \leq Re_\tau \leq 2 \times 10^4$, where Re_τ is defined as $Re_\tau = R/\ell_c$, R is the pipe radius, $\ell_c = \nu/u_\tau$ is the viscous length scale, u_τ is the wall friction velocity,
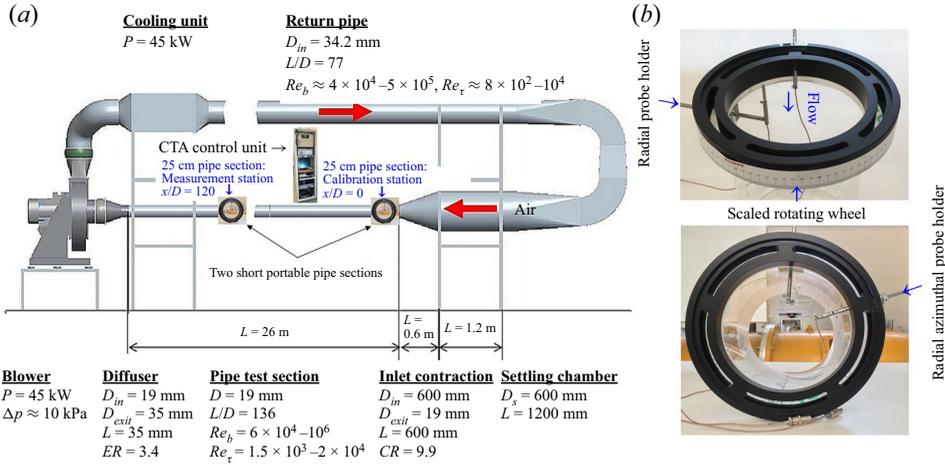
Figure 1. (*a*) The Cottbus large pipe facility. (*b*) The two hot-wire probe module. Here, *CR* is the nozzle contraction ratio, CTA means constant temperature anemometry, *D* is the pipe inner diameter, D_{exit} is the contraction exit diameter, D_{in} is the contraction base diameter, D_s is the settling chamber inner diameter, *ER* is the diffuser expansion ratio, *L* is the pipe/contraction/settling chamber length, *P* is the power, and Δp is the pressure rise.

and ν is the fluid kinematic viscosity. At the pipe inlet, i.e. $x_1/D = 0$, the facility provides air with uniform profiles, i.e. $\bar{U}_1(r) \approx$ constant (figure 2), having turbulence level $\sqrt{\overline{u_1^2}}/\bar{U}_1 \le 0.5\,\%$ (figure 3), where x_1 is the streamwise distance, *D* is the pipe inner diameter, $\bar{U}_1$ is the local mean streamwise velocity, and *r* is the local radial distance. The facility has suction and return pipe sections made out of high-precision smooth acrylic glass with inner diameters 190 ± 0.23 mm and 342 ± 0.35 mm, respectively. The total length *L* of each pipe test section is 26 m, providing length-to-diameter ratios *L/D* of 136 and 77 for the suction and return sections, respectively. Hot-wire anemometry represents the major instrumentation used to carry out measurements. The two hot-wire probe module (figure 1*b*) is utilized to measure the streamwise velocity component at different radial and azimuthal positions. The probe module (figure 1*b*) hosts two hot-wire probes: one probe moves radially, while the other moves in both the radial and the azimuthal directions via a rotating pipe section. Both probe holders are engraved with mm scales to facilitate locating both probes at various wall-normal locations. The rotational pipe section is scaled as well for various azimuthal positions. The azimuthal displacement Δs is calculated based on the angular separation $\Delta \theta$ desired and the local radial distance *r*; $\Delta s/r = (\Delta \theta) \times 2\pi/360$. In this work, all two-point velocity correlations were calculated based on data obtained with the radial probe kept fixed at a preselected pipe wall-normal location while the radial azimuthal probe, located at the same wall-normal distance, was displaced 35–41 times azimuthally between $10°$ minimum and $210°$ maximum separation with step $\Delta \theta = 5°$ with respect to the fixed radial probe.

All experiments in the present study were conducted at four wall-normal locations x_2/R, namely 0.1, 0.2, 0.5 and 0.7 measured from the pipe wall. The wall-normal locations were chosen to have $x_2/R = 0.1$ inside the logarithmic region, $x_2/R = 0.2$ at the top of the logarithmic region, and $x_2/R = 0.5$ and 0.7 in the core region of the pipe. Measurements were performed using Dantec Streamline 9091N0102 constant temperature anemometry (CTA) with commercial Dantec probes, having a sensing element with
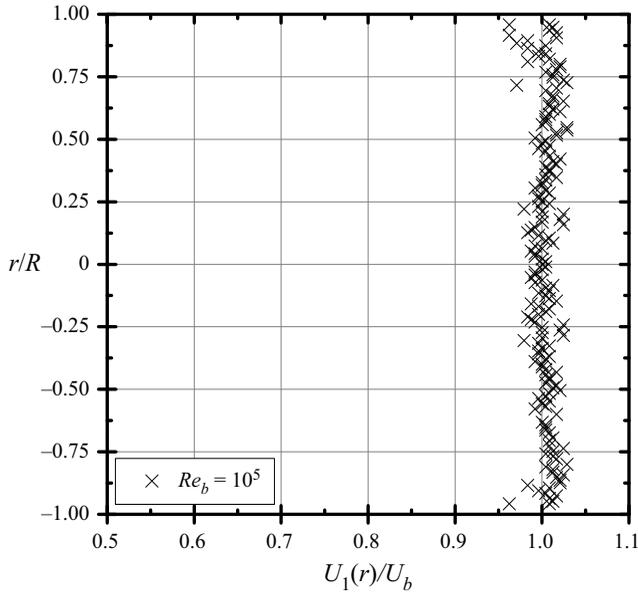
Figure 2. Selected normalized mean velocity profile $\bar{U}_1(r)/\bar{U}_b$ measured at $x_1/D = 0$, using a 2 mm Pitot-static tube, versus the local wall distance r/R for bulk Reynolds number $Re_b = 10^5$ ($Re_\tau \approx 2.2 \times 10^3$).
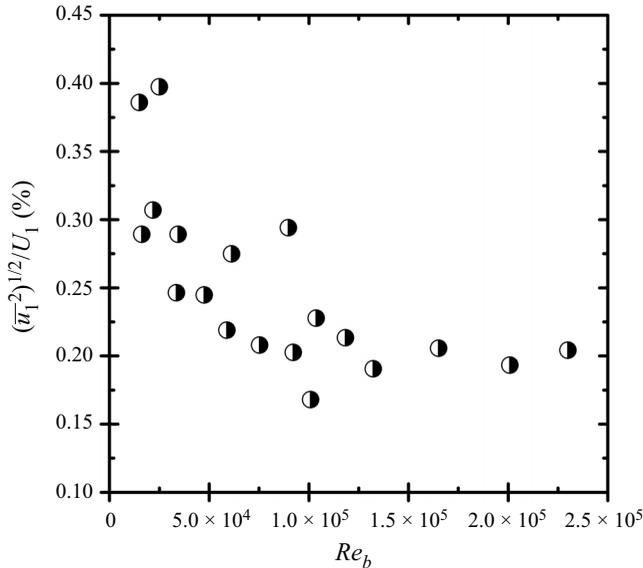
Figure 3. The centreline turbulence level $\sqrt{\overline{u_1^2}}/\bar{U}_1$ measured by hot-wire probe at the pipe inlet for bulk Reynolds numbers $Re_b \leq 2.4 \times 10^5$ ($Re_\tau \leq 5.2 \times 10^3$).

dimensions $\ell \times d = 1250\,\mu\text{m} \times 5\,\mu\text{m}$, where ℓ is the sensor length, and d stands for the sensor diameter. To account for inadequate spatial resolutions of both hot-wire probes, the correction technique proposed by Hutchins *et al.* (2009) for the streamwise velocity fluctuations was adopted with success in the present study. Experiments were conducted with a 30 kHz sampling frequency, providing high enough time-resolved velocity data.

973 A1-6
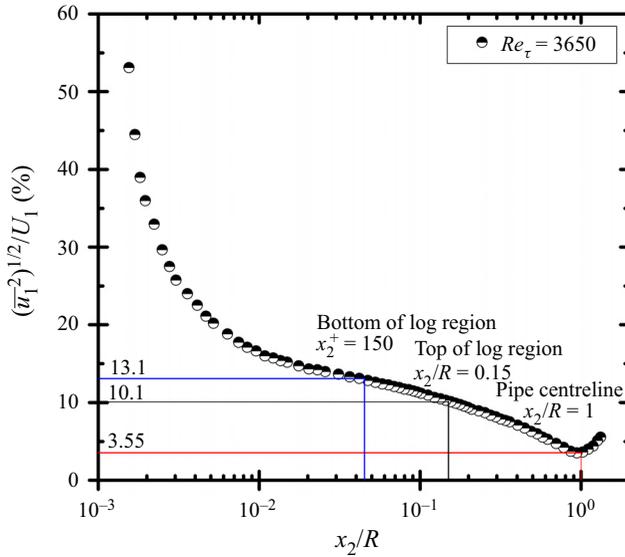
Figure 4. The local turbulence level $\sqrt{\overline{u_1^2}}/\bar{U}_1$ in fully developed turbulent pipe flow regime using a single hot-wire probe for $Re_\tau \approx 3650$.

2.2. *Hot-wire calibration*

Accurate and individual calibration for both hot-wire probes using an appropriate calibration technique is desirable for high-fidelity experimental data. The calibration is to be carried out in a well-defined flow field, i.e. the profile of the local mean velocity $\bar{U}_1(r)$ is uniform (figure 2), with a low turbulence level $\sqrt{\overline{u_1^2}}/\bar{U}_1 \leq 0.5\,\%$ (figure 3), whether *in situ* or *ex situ* calibration is proposed. The *ex situ* calibration might be adopted if the above calibration conditions cannot be fulfilled in the facility that is to be utilized later to carry out further experiments. The *ex situ* calibration, however, has several disadvantages. For instance, the contraction's exit diameter of an external calibrator might not be large enough to host, simultaneously, two hot-wire probes. Thus a sizeable blockage by the two probes in front of the flow field is expected, causing considerable error due to aerodynamic disturbances. In addition, after the completion of the *ex situ* calibration, transferring and integrating both probes into the pipe test section might not be possible.

An alternative approach to an *ex situ* calibration was adopted by Bailey *et al.* (2008), conducting *in situ* calibration at a pipe location where flow was assured to be fully developed turbulent and actual measurements were carried out. It is known, however, that the centreline turbulence level $\sqrt{\overline{u_1^2}}/\bar{U}_1$, as figure 4 shows, for fully developed turbulent pipe flow is approximately 3.5 %, i.e. $\approx$10 times greater than the turbulence level at the pipe inlet test section; see figure 3 and Hinze (1975). To perform such *in situ* calibration for two hot-wire probes, simultaneously, using a Pitot probe located at the pipe centreline, both probes must be positioned offset from the pipe centreline, where the turbulence level is greater than 3.5 % depending on the offset in the wall-normal direction; see figure 4 and table 2.

The high turbulence level received by hot-wire probes during calibration would give rise to substantial levels of uncertainty in measured velocity fluctuations, resulting in error in evaluating the turbulence statistics (Talluru *et al.* 2014; Boufidi *et al.* 2020). For instance, in spectral analysis, the inaccurate hot-wire calibration would result in errors in

Wall-normal distance	$\rightarrow$	$x_2{}^+ = 150$	$x_2/R = 0.15$	$x_2/R = 1$
$\sqrt{\overline{u_1{}^2}}/\bar{U}_1$ (%)	$\rightarrow$	13.1	10.1	3.55

Table 2. The local turbulence level $\sqrt{\overline{u_1{}^2}}/\bar{U}_1$ in fully developed turbulent pipe flow regime for $Re_\tau = 3600$ at various wall-normal locations: $x_2{}^+ = 150$ is the bottom of the logarithmic region, $x_2/R = 0.15$ is the top of the logarithmic region, and $x_2/R = 1$ is the pipe centreline, where $x_2{}^+ = x_2 u_\tau/\nu$.

the estimation of wavenumbers and consequently wavelengths in correspondence with the large-scale motions as well as magnitudes of the spectral peaks.

The present pipe facility provides a unique opportunity to perform precise *in situ* calibration (see e.g. Durst, Zanoun & Pashtrapanska 2001) for both hot-wire probes, simultaneously, with blockage range 0.4 %–2.8 % and minimal aerodynamic disturbances. Two identical 25 cm long portable pipe sections of 190 mm inner diameter were produced (see figure 1*a*). One piece is produced to replace the other that hosts the two hot-wire probes. The one that hosts the two hot-wire probes is presented in figure 1(*b*), allowing the calibration of both probes at the inlet of the pipe test section where the flow is assured to be uniform and laminar for the full range of the Reynolds number, i.e. $6 \times 10^2 < Re_\tau < 2 \times 10^4$, with a very low turbulence level (see figure 3). The streamwise mean velocity component $\bar{U}_1 = \sqrt{2(P_0 - p_{st})/\rho(1 - k)}$ of the air flow at the pipe inlet was obtained via pressure drop $(P_0 - p_{st})$ measurements along the pipe inlet contraction (see figure 1*a*), using a differential pressure transducer and the Bernoulli equation, where ρ is the air density, $k = (D/D_{in})^4$ is the pipe-to-contraction base area ratio, D_{in} is the contraction base diameter, and P_0 and p_{st} are the mean pressures at base and exit of the inlet contraction, respectively. After the calibration data acquisition $\bar{E} = f(\bar{U}_1)$, a fourth-degree polynomial was chosen to fit the calibration data for each hot-wire probe, with least-squares error better than ± 1 % (see figure 5), where $\bar{E}$ is the mean hot-wire output. After ensuring high-precision calibration for the two hot-wire probes at the pipe inlet, the CTA control unit was set to standby. Then the pipe segment that hosts the two hot-wire probes was completely transferred to the measurement station at $x_2/D = 120$, where the pipe flow was assured to be fully developed turbulent, and the CTA was set back to on. To ensure that the original calibration curve was maintained during one entire set of measurements, the calibration curves were rechecked after each set of measurements covering the entire range of velocities experienced. It is worth noting that each hot-wire probe was integrated with a 20 m long PNC cable, i.e. 105 pipe diameters, connecting it to the CTA. In addition, the CTA control unit was set up on a movable cabinet that is located near the middle of the pipe facility, i.e. at length $\approx$70 pipe diameters from the pipe inlet. Thus the set-up allows exchanging the two hot-wire probe module between the pipe inlet $x_1/D = 0$ and the measurement station at $x_1/D = 120$ without disconnecting them.

To summarize, the inconsistencies observed in the available two-point correlation hot-wire data in literature might be attributed to:

(i) uncertainties in the calibration of hot-wire probes due to difficulties in conducting simultaneous *in situ* calibration, resulting in errors in the statistical analysis and in the conclusions drawn;

(ii) at high Reynolds numbers, inadequate spatial (Blackwelder & Haritonidis 1983; Hutchins *et al.* 2009) and temporal (Hutchins *et al.* 2015) resolutions, in particular,
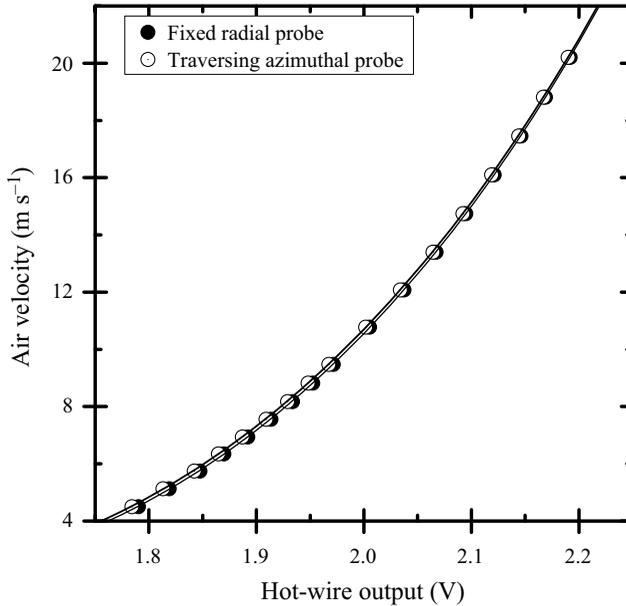
Figure 5. The calibration curves for both hot-wire probes with least-squares errors 0.25 % and 0.27 % for the radial and azimuthal probes, respectively.

in the vicinity of the wall where the flow exhibits a strong gradient, introducing an additional source of error in the calibration equation and in the statistical analysis;

(iii) temperature drift (Talluru *et al.* 2014) and uncertainties in positioning both probes with respect to the pipe wall (Örlü, Fransson & Alfredsson 2010), also of importance during the calibration and measurements.

The present work was therefore undertaken with the aim of obtaining accurate pipe flow data, utilizing the CoLaPipe in the fully developed turbulent flow regime for $2 \times 10^3 \leq Re_\tau \leq 16 \times 10^3$ and wall-normal distances $0.1 \leq x_2/R \leq 0.7$.

3. Data analysis

3.1. *Uncertainty and energy spectra*

We start by examining briefly the measurement uncertainty that might be introduced into the streamwise velocity component due to the blockage of the probe holders and probable eccentricity of the hot-wire probes. The blockage of the pipe cross-section due to probe holders ranged from 0.4 % to 2.8 % for wall-normal locations $x_2/R = 0.1$ and $x_2/R = 0.7$, respectively. The experimental deviations in the local mean and fluctuations of the streamwise velocity component obtained from both hot-wire probes were examined at the four wall-normal locations $x_2/R = 0.1, 0.2, 0.5, 0.7$ and the 35–41 azimuthal positions. Selected samples at the wall-normal locations $x_2/R = 0.1$ and $x_2/R = 0.7$, representing the minimum and maximum blockages, respectively, are shown in figure 6 for two different Reynolds numbers.

For each measure, the two probes were located at the same wall-normal distance, therefore both probes are expected to receive and measure the same local time-averaged and higher-order statistics of the streamwise velocity component for all azimuthal positions. Using the least-squares method, figures 6(*a*,*b*) illustrate an uncertainty/deviation
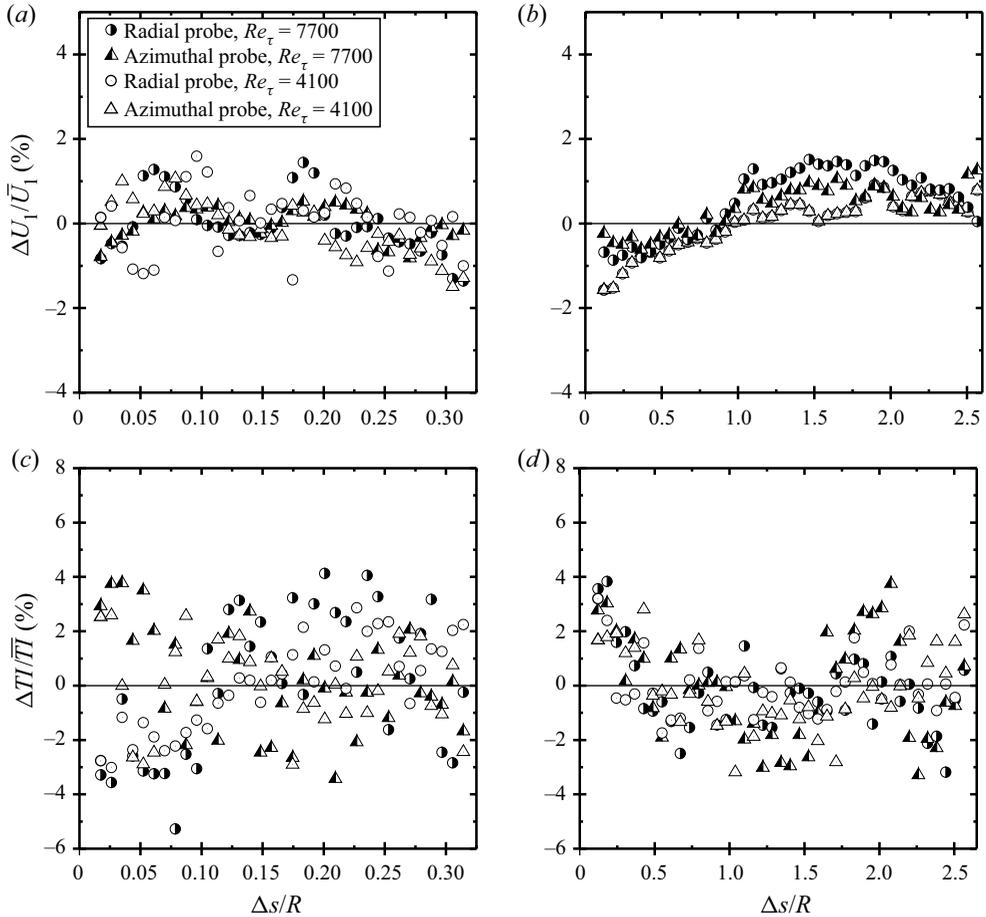
Figure 6. The local deviation in the streamwise velocity component (*a*,*b*) mean and (*c*,*d*) fluctuations at two wall-normal locations of the pipe cross-section, and two Reynolds numbers: (*a*,*c*) $x_2/R = 0.1$ (0.4 % blockage) and (*b*,*d*) $x_2/R = 0.7$ (2.8 % blockage).

$\Delta U_1/\bar{U}_1$ within the range $\pm 0.4\%$ to $\pm 1.6\%$ in the local mean velocity obtained from either the fixed or the traversing azimuthal hot-wire probes at $x_2/R = 0.1, 0.7$, respectively. Note that the deviation in the local mean is defined as $\Delta U_1/\bar{U}_1 = (U_1 - \bar{U}_1)/(\bar{U}_1)$, where U_1 is the individual local mean of the streamwise velocity component, and $\bar{U}_1$ represents the average of all local means of the streamwise velocity component across all azimuthal locations. On the other hand, figures 6(*c*,*d*) show the uncertainty/deviation in the turbulence intensity level $TI = \sqrt{\overline{u_1^2}}/U_1$ for the streamwise velocity component from both probes, with average values within the range $\pm 0.7\%$ to $\pm 2.67\%$ based on the least-squares method at $x_2/R = 0.1, 0.7$, respectively. Note also that the deviation in TI is defined as $\Delta TI/\overline{TI} = (TI - \overline{TI})/(\overline{TI})$, where TI is the individual local turbulence intensity level, and $\overline{TI}$ represents the average of all local values of TI across all azimuthal locations. The small discrepancies observed in figure 6 between the two probes might be attributed to aerodynamic interference effects between the two probes, regardless of the separation, i.e. $\Delta\theta$, as well as to some probe eccentricity. The local turbulence intensity TI levels received from either the fixed or the traversing azimuthal probes at the

four wall-normal locations agree well with similar data presented earlier in figure 4 and obtained from a single hot-wire probe at various wall-normal locations.

To further assess effects of probe-holder blockage and/or probe eccentricity on the present pipe data analysis, the streamwise energy spectra measured at 35–41 azimuthal positions were calculated versus spectra measured 35–41 times at identical locations and a pre-selected wall-normal location for the same Reynolds number. The solid line presented in each spectrum subplot in both figures 7 and 8 represents the average across all azimuthal locations between the minimum probe separation $\Delta \theta = 10°$ and the maximum probe separation $\Delta \theta = 210°$. All power-spectral dashed lines presented in both figures 7 and 8 were obtained in a similar manner to the solid lines, representing the average for all measured cases, utilizing the radial probe at the same radial location. It is worth noting here that the frequency spectra $\Phi_{u_1 u_1}(f)$ were estimated using Welch's power-spectral density method, i.e. fast Fourier transform. The time trace data of the streamwise velocity fluctuations received from each hot-wire probe were acquired at a $30\,\text{kHz}$ sampling frequency with a 60–120 sampling time, providing a total number of 1.8–3.6×10^6 samples (see table 1). The data were then divided into eight successive blocks with 50 % overlap, and each segment was windowed with a Hamming window. Thereafter, to map the frequency spectra $\Phi_{u_1 u_1}(f)$ into the wavenumber spectra $\Phi_{u_1 u_1}(k_{x_1})$, Taylor's convected frozen-turbulence hypothesis

$$\frac{\partial}{\partial x_1} = -\frac{1}{\bar{U}_1(x_2)} \frac{\partial}{\partial t} \quad \longrightarrow \quad k_{x_1} = 2\pi \frac{f}{\bar{U}_1(x_2)} \tag{3.1}$$

was implemented (Taylor 1938), assuming convection of the pipe flow structure with the local mean velocity (for more details, see de Kat & Ganapathisubramani 2015).

Note that Taylor's hypothesis relates the longitudinal spatial correlation to the temporal correlation at a single point measured by the hot-wire probe. Thus the wavenumber relation $k_{x_1} = 2\pi f/\bar{U}_1(x_2)$ converts the spectral argument from the frequency domain f to the wavenumber k_{x_1} domain, where k_{x_1} is the streamwise wavenumber, and $\bar{U}_1(x_2)$ is the local mean convective streamwise velocity. The streamwise spectra $\Phi_{u_1 u_1}(k_{x_1})$ are scaled with the wall friction velocity u_τ (Zanoun *et al.* 2021), the streamwise wavelength k_{x_1} and the pipe radius R, resulting in the so-called premultiplied spectra $k_{x_1} R\, \Phi_{u_1 u_1}(k_{x_1})/u_\tau^2 \equiv k_{x_1} R \Phi_{u_1 u_1}^{++}$ presented in both figures 7 and 8 versus the normalized wavenumber $k_{x_1} R$. Both figures show satisfactory collapse of the premultiplied spectra lines obtained from the two hot-wire probes at pre-selected wall-normal locations and Reynolds numbers. The small differences observed between the two hot-wire probes, $x_2/R = 0.1$ in figure 7(*a*) and $x_2/R = 0.2$ in figure 7(*b*), might either reflect changes in the azimuthal structure of the large-scale motions, in particular, in the inner wall layer as will be shown later, or be due to the wall interaction with both the radial and azimuthal probes. The amplitudes of the peaks observed in the energy spectra of the two probes in both figures agree within ± 1.5 % to ± 5 %, indicating minimal effects of the blockage due to probe holders and/or probe eccentricity. In both figures 7 and 8, two discernible peaks are observable: one at low streamwise wavenumber associated with the very-large-scale motion (VLSM), and the second at moderate streamwise wavenumber associated with the large-scale motion (LSM). The two observable peaks in the energy spectra obtained at low and moderate wavenumbers are clear evidence or footprints for the LSMs in the pipe flow. Thus the two modes, i.e. a low-wavenumber mode and moderate-wavenumber mode, adopted from both figures 7 and 8 are in agreement with Kim & Adrian (1999) for the pipe flow. The VLSMs and LSMs are located at the streamwise wavenumbers $k_{x_1} R \approx 0.4$–1
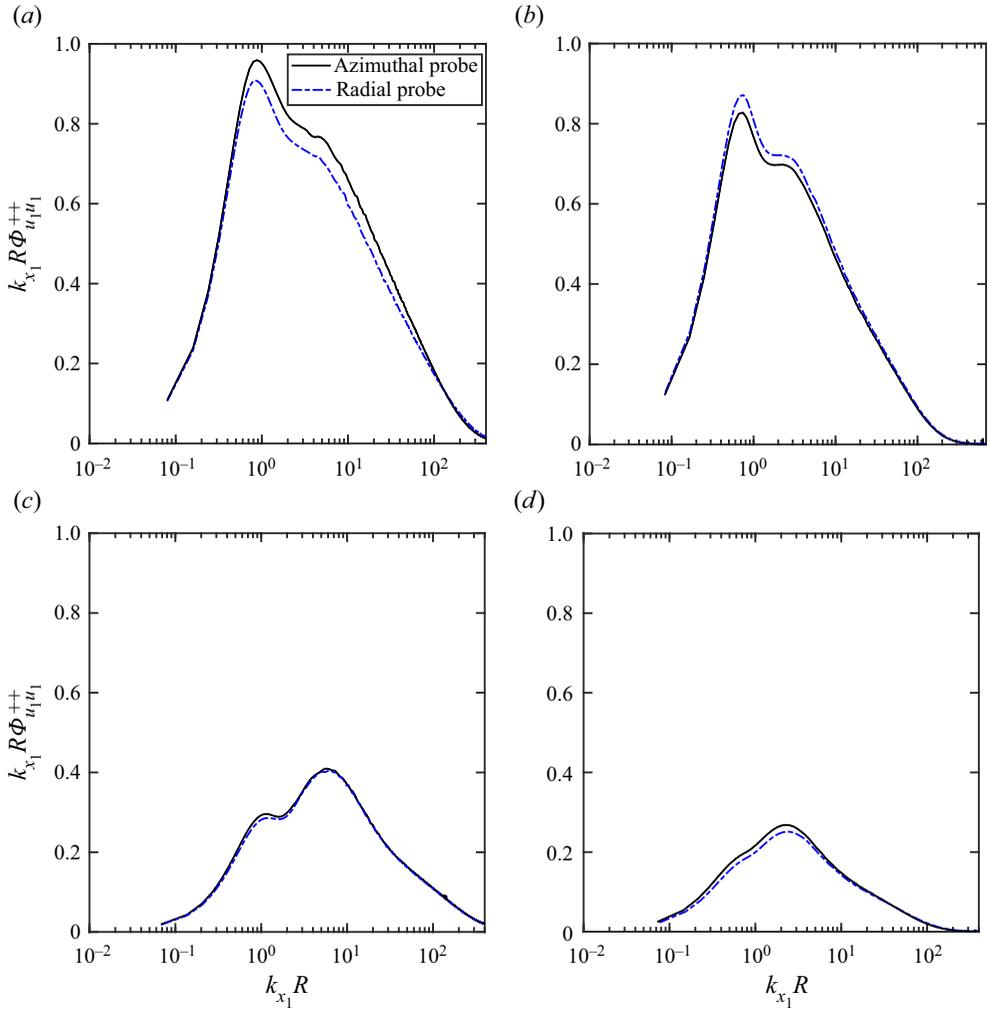
Figure 7. Effect of wall-normal location x_2/R. Premultiplied energy spectra $k_{x_1} R \Phi_{u_1 u_1}^{++}$ in outer scaling versus the streamwise normalized wavenumber $k_{x_1} R$ for shear Reynolds number $Re_\tau \approx 4100$: (*a*) $x_2/R = 0.1$, (*b*) $x_2/R = 0.2$, (*c*) $x_2/R = 0.5$, and (*d*) $x_2/R = 0.7$.

and $k_{x_1} R \approx 2$–6, respectively, in alignment with Kim & Adrian (1999) and Balakumar & Adrian (2007). One can observe from $x_2/R = 0.1$ in figure 7(*a*) and $x_2/R = 0.2$ in figure 7(*b*) that the inner peak, representing the VLSM, is more prominent than the outer peak of the LSM, in agreement with a similar observation made by Kim & Adrian (1999) and Bailey *et al.* (2008). Both peaks decrease in energy content with increase in the wall-normal distance, as indicated for $x_2/R = 0.5$ in figure 7(*c*) and $x_2/R = 0.7$ in figure 7(*d*); however, the energy contained in the VLSM peak decreases faster than that for the LSM. On the other hand, the LSM peak observed in figures 7(*c*) and (*d*) ($x_2/R = 0.5$ and $x_2/R = 0.7$, respectively), i.e. in the core region, is more prominent than the VLSM peak. The VLSMs seem from figure 7(*c*) to continue until $x_2/R = 0.5$, and thereafter one large-scale structure forms, i.e. LSM structures, and extends to the pipe centreline, as will be shown later. The physical model proposed by Kim & Adrian

973 A1-12
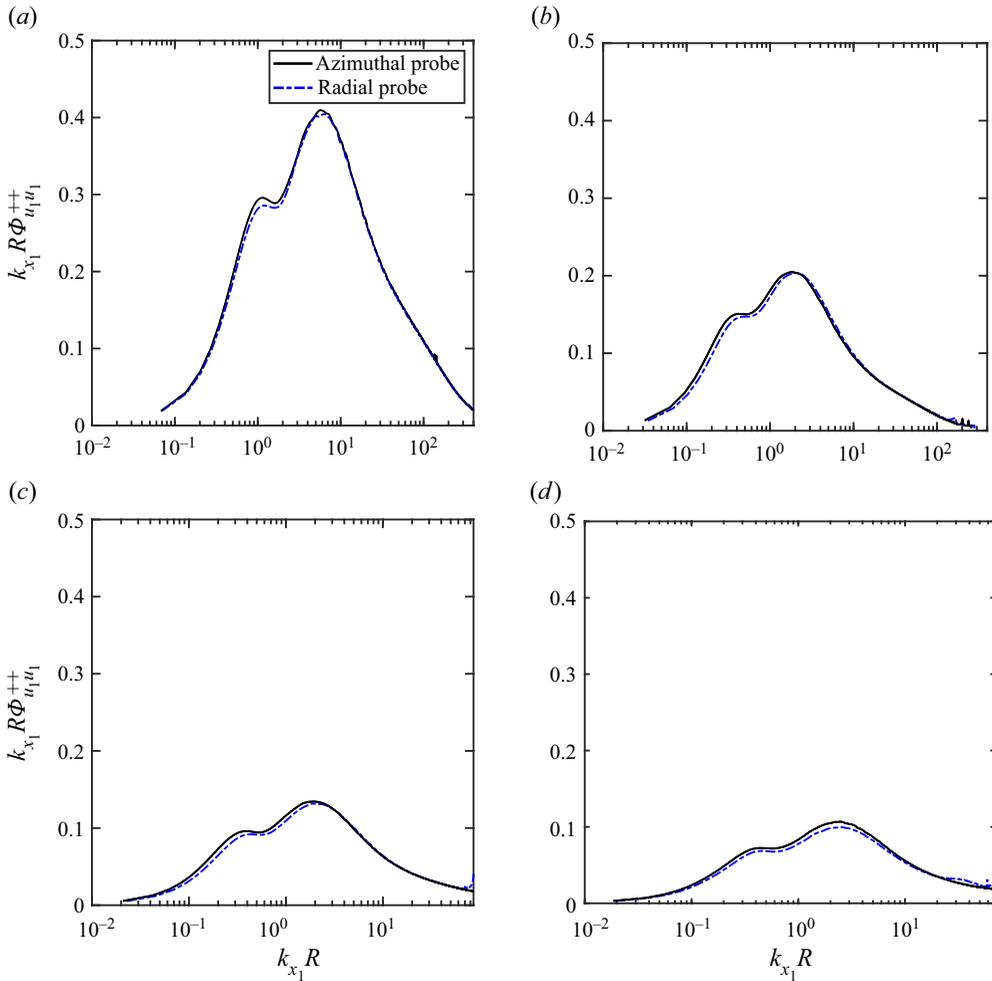
Figure 8. Effect of the Reynolds number Re_τ. Premultiplied energy spectra $k_{x_1} R \Phi_{u_1 u_1}^{++}$ in outer scaling versus the streamwise normalized wavenumber $k_{x_1} R$ at a wall-normal location $x_2/R = 0.5$: (*a*) $Re_\tau = 4100$, (*b*) $Re_\tau = 7700$, (*c*) $Re_\tau = 11\,500$, and (*d*) $Re_\tau = 15\,300$.

(1999) and Meinhart & Adrian (1995) – that the VLSMs are associated with the zones of uniform low momentum found in the boundary layer that extend only up to approximately one-half of the boundary layer thickness or the pipe radius – would be appropriate to interpret the disappearance of the VLSMs peak beyond $x_2/R = 0.5$ as indicated in figure 7(*d*).

To study further the effect of the Reynolds number on both the inner and outer peaks of the LSMs, a selected sample is presented in figure 8 at $x_2/R = 0.5$ for $4100 \leq Re_\tau \leq 15\,300$. The overall behaviour is similar in all plots in terms of the appearance of the inner and outer peaks and their wavenumbers. However, a clear dependence of the magnitude of the energy peaks at the corresponding wavenumbers for the LSM and VLSM on the Reynolds number is observable.

3.2. *Azimuthal velocity correlation*

To characterize the azimuthal pipe flow structure, the two-point velocity correlation coefficient $R_{u_1u_1}(\Delta s)$, defined in § 1, was calculated and illustrated in both figures 9 and 10, addressing the effect of the wall-normal location, the azimuthal separation, and the Reynolds number on $R_{u_1u_1}(\Delta s)$. Both figures represent profiles of $R_{u_1u_1}(\Delta s)$ obtained at four wall-normal locations, $x_2/R = 0.1, 0.2, 0.5, 0.7$, for 35–41 azimuthal positions and Reynolds numbers in the range $4100 \leq Re_\tau \leq 15\,300$.

It is worth noting that the wall-normal locations were chosen to show changes in the azimuthal structure in both the logarithmic and core regions of the fully developed turbulent pipe flow. In figure 9, for small azimuthal separation distances between the two hot-wire probes, high correlation values were obtained, indicating strong coherence between the two signals where both probes would receive velocity fluctuations with similar signs. By increasing the azimuthal separation distance between the two probes, the coherence is weakened, reaching zero at various separation distances, depending on the wall-normal location and the Reynolds number, and then its sign changes to negative. All plots of the figure illustrate regions of positive–negative velocity correlations within various ranges of $\Delta s/R$, expressing clear dependence on the wall-normal location, the azimuthal separation and the Reynolds number. The positive–negative trends of the correlation coefficient shown in figure 9 represent an indication of the vortex-packets/hairpin pipe flow structure in agreement with similar observations made by Tomkins & Adrian (2003) and Monty *et al.* (2007) for flat-plate boundary layer and pipe flows, respectively.

Each plot in figure 9 presents the azimuthal velocity correlation $R_{u_1u_1}(\Delta s)$ at four wall-normal locations, $x_2/R = 0.1, 0.2, 0.5, 0.7$, for similar Reynolds numbers, namely, $Re_\tau = 4100$ (figure 9a), $Re_\tau = 7700$ (figure 9b), $Re_\tau = 11\,500$ (figure 9c) and $Re_\tau = 15\,300$ (figure 9d). The positive–negative values obtained are attributed to the azimuthal LSMs in alignment with the earlier definition of the LSMs as scales that produce energetic flow motions of long meandering positive-negative velocity fluctuations, see Tomkins & Adrian (2003) and Monty *et al.* (2007). It turns out to be also in alignment with Bailey *et al.* (2008), who reported that the negative values of $R_{u_1u_1}(\Delta s)$ obtained for the pipe flow can be attributed to the contribution of the LSMs to the coherent structure. For similar Reynolds numbers, changes in the magnitude and the range of the negative values of $R_{u_1u_1}(\Delta s)$ for the various wall-normal locations observed in figure 9 reflect a clear dependence of the azimuthal scales of the LSMs on the wall-normal location.

From a first look, it seems from figures 9(*a–d*), however, that the Reynolds number effect is not predictable. Near the wall, i.e. $x_2/R = 0.1, 0.2$, the two-point correlation function $R_{u_1u_1}(\Delta s)$ narrows in figures 9(*c,d*) for $Re_\tau = 11\,500, 15\,300$, while it broadens in figures 9(*a,b*) for $Re_\tau = 4100, 7700$, respectively. At high Reynolds numbers, the measured velocity signals were attenuated, and due to the averaging process introduced into (1.1) over a wide range of turbulence scales, the *Re* dependence was not properly revealed in figure 9. The cross-power spectral density is thus introduced in § 3.3 to highlight the Reynolds number effects on the azimuthal length scales at various wall-normal locations. However, figure 10 is produced here to see whether the azimuthal velocity correlation data presented in figure 9 are dependent only on the wall-normal location and the azimuthal separation.

Figure 10 is an isocontour plot of the azimuthal velocity correlation $R_{u_1u_1}(\Delta s)$ for the four Reynolds numbers reported earlier at the wall-normal locations $0.1 \leq x_2/R \leq 0.7$. The figure allows better visualization for the effect of the Reynolds number on $R_{u_1u_1}(\Delta s)$

across the pipe versus the azimuthal separations (Δs) for the wall-normal locations reported in figure 9. Due to axisymmetry of the pipe flow, it is worth noting that the data presented in figure 10 are for $0° \leq \Delta\theta \leq 180°$ and imaged to the second half of the pipe cross-section. The contours and the colour levels in all plots are similar, i.e. the colour indicates the magnitude of $R_{u_1 u_1}(\Delta s)$ given by the scale at the right of the plot. Qualitatively, the overall views of all four plots are similar; however, with deeper insight one can observe differences among all four plots, indicating a Reynolds number dependence, in disagreement with Bailey *et al.* (2008), who reported Reynolds number independence for the correlation coefficient. Figure 10 is believed to be more illustrative, indicating slight dependence of the two-point velocity correlation on the Reynolds number, the wall-normal distance and the azimuthal separation.

To better highlight the Reynolds number effects at various wall-normal locations, the cross-power spectral analysis is introduced in the next subsection. It might be noted, however, that slightly positive correlation values observed in figure 10 at large azimuthal separation and low Reynolds number would reflect possible flow periodicity in agreement with the conclusion made by Bailey *et al.* (2008). More analysis to quantify the sizes of the azimuthal scales of the LSMs for the present Reynolds number range $4100 \leq Re_\tau \leq 15\,300$ and the wall-normal distances $0.1 \leq x_2/R \leq 0.7$ is discussed in the following subsection.

3.3. *Cross-power spectral density*

In principle, the cross-correlation and cross-power spectral density functions are pairs of Fourier transforms. For specific purposes, one form is often preferred over the other, for instance, when the contribution of the LSMs and VLSMs to the azimuthal scale structures is to be evaluated. The velocity cross-correlation $R_{u_1 u_1}(\Delta s)$ data illustrated in both figures 9 and 10 were estimated using (1.1), which was defined based on ensemble averaging of the hot-wire data, comprising contributions from a broad band of turbulence scales that mix the contributions of all wavenumbers to the azimuthal pipe LSMs. It was concluded by Bailey *et al.* (2008) that the averaging introduced in (1.1) obscures the proper contributions of both the LSMs and the VLSMs to the azimuthal scales. Thus the cross-power spectral density $G(\Delta s, k_{x_1})$ for the streamwise velocity fluctuations as a function of the azimuthal separation Δs and the streamwise wavenumber k_{x_1} was proposed (Bailey *et al.* 2008), to overcome the averaging introduced in (1.1). The cross-power spectral density $G(\Delta s, k_{x_1})$ is defined as

$$G(\Delta s, k_{x_1}) = F^*(0, k_{x_1})\, F(\Delta s, k_{x_1}), \tag{3.2}$$

where $G(\Delta s, k_{x_1})$ is calculated using Welch's averaging method, i.e. a modified periodogram method of spectral estimation. It is the fast Fourier transform of the cross-correlation function between the two signals recorded by the two hot-wire probes, simultaneously, each of sampling size indicated in table 1. It is worth noting that the cross-power spectral density is single-sided, yielding information about the power/energy shared over a range of wavenumbers as well as the coherence or the phase difference between the two signals received from the two hot-wire probes. It is therefore used to specify the power/energy shared at specific flow wavenumbers, for instance, corresponding to the LSM and the VLSM of the streamwise velocity fluctuations. The quantity $F^*(0, k_{x_1})$ is a complex conjugate of the finite Fourier transform of the streamwise velocity fluctuations $u_1(0, t)$ measured by the fixed radial probe, while $F(\Delta s, k_{x_1})$ is the finite Fourier transform of the streamwise velocity fluctuations $u_1(\Delta s, t)$ measured by the
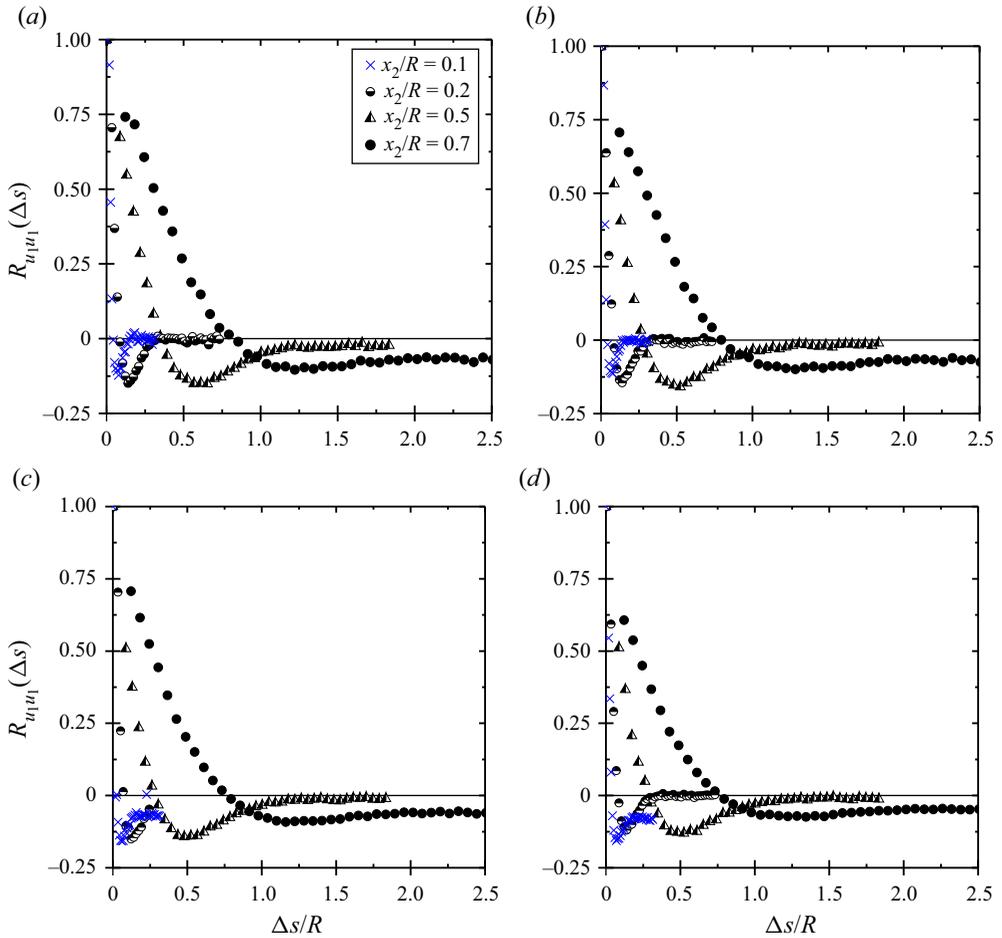
Figure 9. Effect of the wall-normal location x_2/R, the azimuthal separation $\Delta s/R$ and the Reynolds number Re_τ on the azimuthal velocity correlation $R_{u_1 u_1}(\Delta s)$ of the streamwise velocity fluctuations at four wall-normal locations, $0.1 \leq x_2/R \leq 0.7$ and $4100 \leq Re_\tau \leq 15\,300$: (*a*) $Re_\tau = 4100$, (*b*) $Re_\tau = 7700$, (*c*) $Re_\tau = 11\,500$, and (*d*) $Re_\tau = 15\,300$.

traversing azimuthal probe. The real component $\Psi(\Delta s, k_{x_1})$ of the cross-power spectral density $G(\Delta s, k_{x_1})$, defined as

$$\Psi(\Delta s, k_{x_1}) = \mathrm{Re}[G(\Delta s, k_{x_1})] \sqrt{\langle u_1^2(0, t)\rangle} \sqrt{\langle u_1^2(\Delta s, t)\rangle}, \tag{3.3}$$

is extracted and used to discuss further the distribution of the correlation of the streamwise velocity fluctuations as a function of the azimuthal separation Δs and the streamwise wavenumber k_{x_1} for various Reynolds numbers and wall-normal locations. On the other hand, the imaginary part of the cross-power spectral density function indicates whether the signals received from the two hot-wire probes are in phase or not. If both signals are in phase, then the cross-power spectral density is positive, while if they are $\pm 180°$ out of phase, then the cross-power spectral density is negative.

Figures 11 and 12 represent in outer scaling the real component $\Psi(\Delta s, k_{x_1})$ of the cross-power spectral density normalized using the streamwise wavenumber k_{x_1}, the pipe radius R and the wall friction velocity u_τ, resulting in the so-called premultiplied

(*a*)

(*b*)

(*c*)

(*d*)
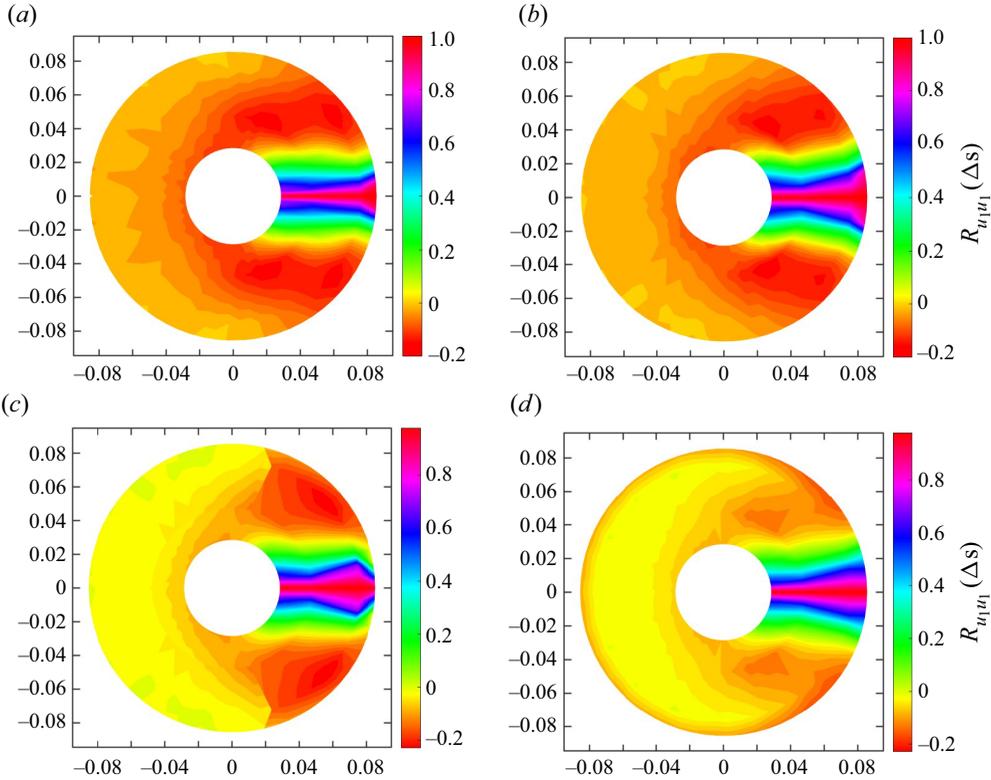
Figure 10. Effect of the wall-normal location x_2/R, the azimuthal separation $\Delta s/R$ and the Reynolds number Re_τ on the azimuthal velocity correlation $R_{u_1u_1}(\Delta s)$. Isocontours of the azimuthal correlation of the streamwise velocity component $R_{u_1u_1}(\Delta s)$ at four wall-normal locations, $0.1 \leq x_2/R \leq 0.7$ and $4100 \leq Re_\tau \leq 15\,300$: (*a*) $Re_\tau = 4100$, (*b*) $Re_\tau = 7700$, (*c*) $Re_\tau = 11\,500$, and (*d*) $Re_\tau = 15\,300$.

cross-power spectral density $k_{x_1} R \, \Psi(\Delta s, k_{x_1})/u_\tau u_\tau \equiv k_{x_1} R \Psi_{u_1 u_1}^{++}$, versus the streamwise wavenumber k_{x_1} normalized with the pipe radius R, i.e. $k_{x_1} R$. Both figures 11 and 12 reflect the effect of the Reynolds number and the wall-normal location, respectively, on premultiplied cross-power spectral density $k_{x_1} R \Psi_{u_1 u_1}^{++}$. At fixed wall-normal location $x_2/R = 0.7$, figure 11 presents $k_{x_1} R \Psi_{u_1 u_1}^{++}$ versus $k_{x_1} R$ for various azimuthal separations $10^\circ \leq \Delta\theta \leq 210^\circ$ and Reynolds numbers $4100 \leq Re_\tau \leq 15\,300$. The figure shows a dependence of the peak–trough values of $k_{x_1} R \Psi_{u_1 u_1}^{++}$ and consequently the azimuthal structures on the Reynolds number as well as on the azimuthal separation for a fixed wall-normal location $x_2/R = 0.7$. Further, figure 12 illustrates $k_{x_1} R \Psi_{u_1 u_1}^{++}$ versus the normalized streamwise wavenumber $k_{x_1} R$ at four wall-normal locations $0.1 \leq x_2/R \leq 0.7$ for various azimuthal separations $10^\circ \leq \Delta\theta \leq 210^\circ$ and selected Reynolds number $Re_\tau = 4100$. In both figures, the decrease in plot-line thickness as well as the downward arrow on all subplots indicate the direction of increasing azimuthal separation $\Delta\theta$ between the two probes. Figure 12 indicates a peak–trough mode with comparable behaviour for the wall-normal locations $x_2/R = 0.1, 0.2$. In all four plots, the peak of $k_{x_1} R \Psi_{u_1 u_1}^{++}$ attenuates with increasing the azimuthal separation $\Delta\theta$ between the two probes, and the rate of attenuation/decay is higher for the closest pipe wall-normal locations $x_2/R = 0.1, 0.2$, where the hot-wire probes in both plots belong to the logarithmic layer. For similar Reynolds number $Re_\tau = 4100$, the peak value of $k_{x_1} R \Psi_{u_1 u_1}^{++}$ attenuates quickly with

973 A1-17
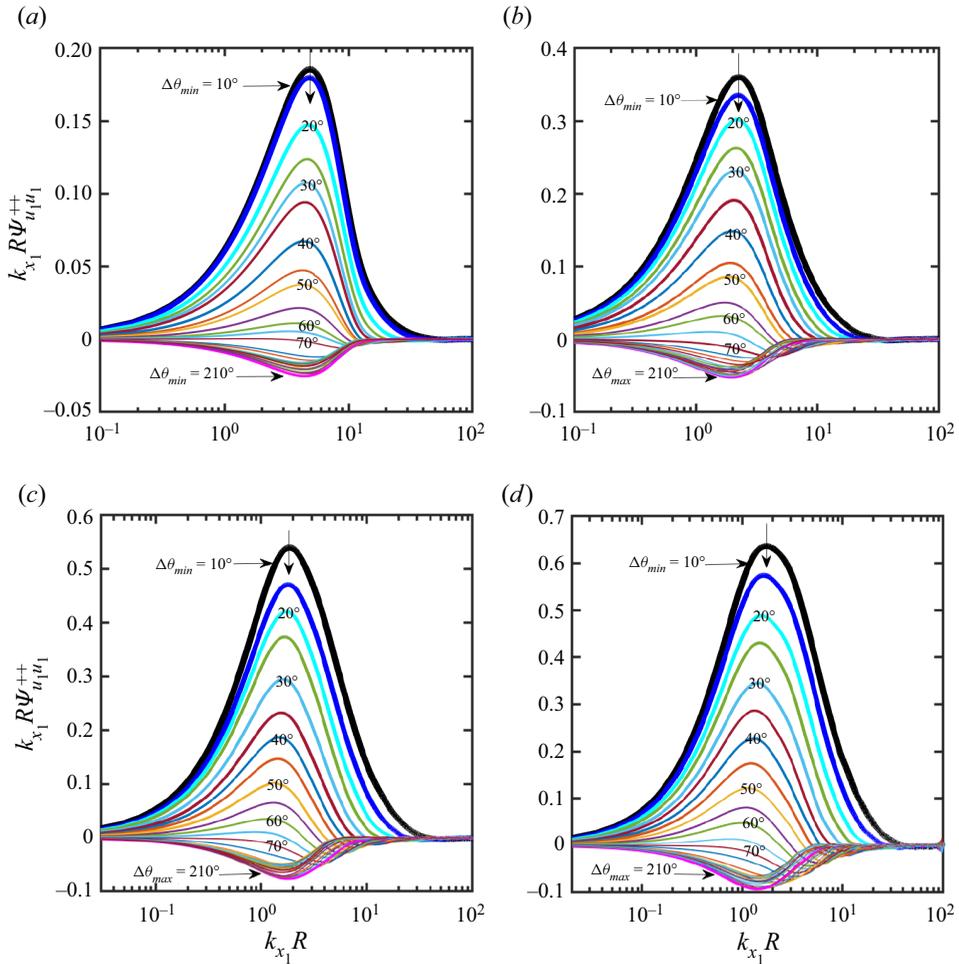
Figure 11. Effect of Reynolds number on premultiplied cross-power spectral density $k_{x_1} R\Psi_{u_1 u_1}^{++}$ at fixed wall-normal location $x_2/R = 0.7$. The downward arrow indicates increasing azimuthal separation $\Delta\theta$ between the two hot-wire probes. Plots are for $x_2/R = 0.7$ and (a) $Re_\tau = 4100$, (b) $Re_\tau = 7700$, (c) $Re_\tau = 11\,500$, and (d) $Re_\tau = 15\,300$.

increasing both the azimuthal separation $\Delta\theta$ and the wall-normal location x_2/R; in particular, see figures 12(a–c) for $0.1 \le x_2/R \le 0.5$ up to azimuthal separation $\Delta\theta \approx 45°$. Changes in trough/negative values are also observable versus both the wall-normal location and the azimuthal separations. Those observations would be considered good indications of the coherence weaknesses as the azimuthal separation and the wall-normal locations increase. For the low Reynolds number cases, the viscous effect, in particular, near the pipe wall play an important role, contrary to the higher Reynolds number cases. Such rapid decay observed in $(k_{x_1} R\Psi_{u_1 u_1}^{++})_{peak}$ might also be interpreted by the hairpin vortex model proposed by Theodorsen (1952). On the contrary, figures 11(d) and 12(d) for $x_2/R = 0.7$ showed slow decay rate in $(k_{x_1} R\Psi_{u_1 u_1}^{++})_{peak}$ versus the azimuthal separation $\Delta\theta$, which could be attributed to the relatively long lifetimes of the azimuthal vortices found predominantly in the core region compared to figures 11(a–c) and 12(a–c).

To further support the data presented in figures 11 and 12, figures 13 and 14 are produced. Both figures 13 and 14 depict in outer scaling the isocontours of the real-part of

973 A1-18
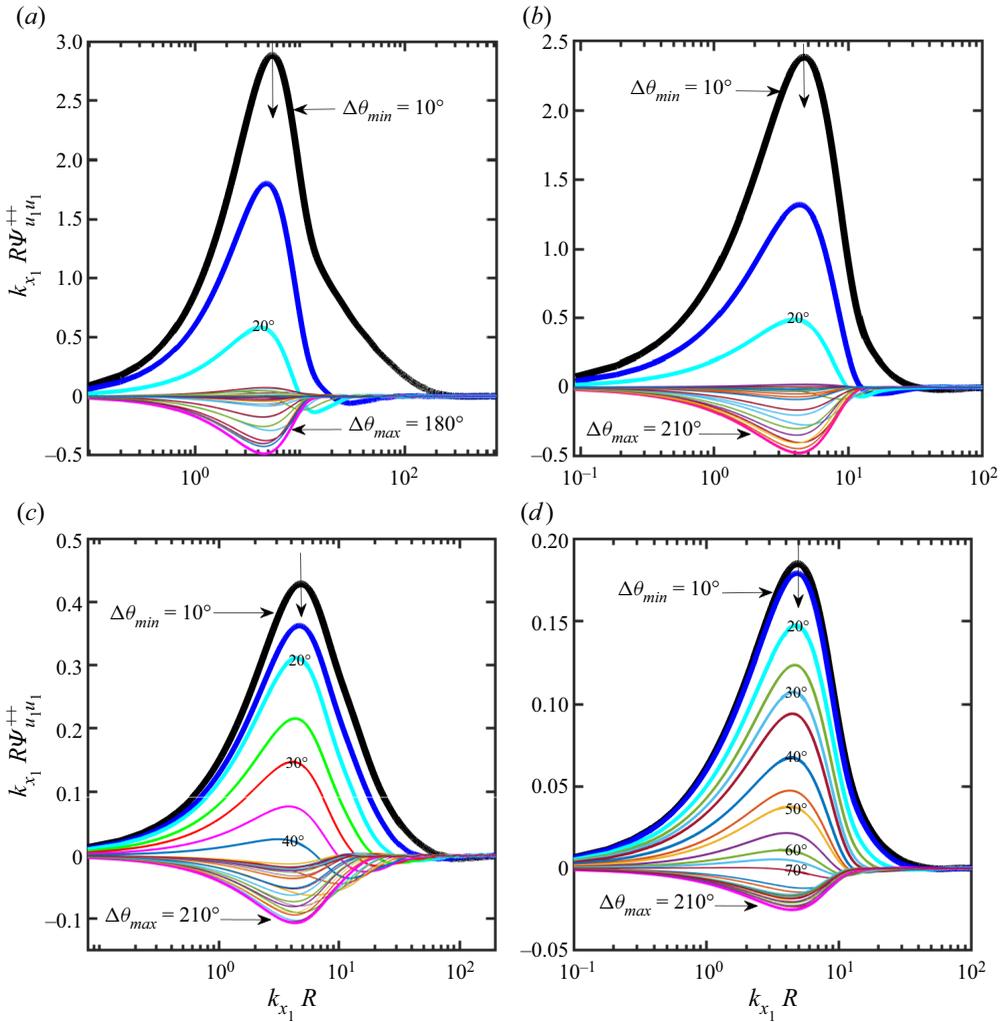
Figure 12. Effect of wall-normal location x_2/R on premultiplied cross-power spectral density $k_{x_1} R \Psi_{u_1 u_1}^{++}$ for constant Reynolds number $Re_\tau = 4100$. The downward arrow indicates increasing azimuthal separation $\Delta\theta$. Plots are for $Re_\tau = 4100$ and (*a*) $x_2/R = 0.1$, (*b*) $x_2/R = 0.2$, (*c*) $x_2/R = 0.5$, and (*d*) $x_2/R = 0.7$.

premultiplied cross-power spectral density $k_{x_1} R \Psi_{u_1 u_1}^{++}$ versus the streamwise wavenumber normalized $k_{x_1} R$. Figure 13 presents isocontours of $k_{x_1} R \Psi_{u_1 u_1}^{++}$ versus $k_{x_1} R$ at $x_2/R = 0.7$ for $4100 \leq Re_\tau \leq 15\,300$ and $10° \leq \Delta\theta \leq 210°$. Similar to figure 11, figure 13 shows a clear dependence of the peak of $k_{x_1} R \Psi_{u_1 u_1}^{++}$ on the Reynolds number as well as on the azimuthal separation for fixed wall-normal location. For the four wall-normal locations $x_2/R = 0.1, 0.2, 0.5, 0.7$, figures 14(*a–d*) were produced, representing isocontours of $k_{x_1} R \Psi_{u_1 u_1}^{++}$ for $Re_\tau = 4100$. The figure allows, for the same Reynolds number, better visualization of the effect of changing the wall-normal position and the azimuthal separation on $k_{x_1} R \Psi_{u_1 u_1}^{++}$. One would, clearly, observe the regions of positive and negative values of $k_{x_1} R \Psi_{u_1 u_1}^{++}$ over various ranges of the azimuthal probe separation $\Delta\theta$. Mostly, the negatively correlated signals occur at low and moderate streamwise wavenumbers $k_{x_1} R$ – however, at large enough azimuthal probe separation. The positive–negative values of
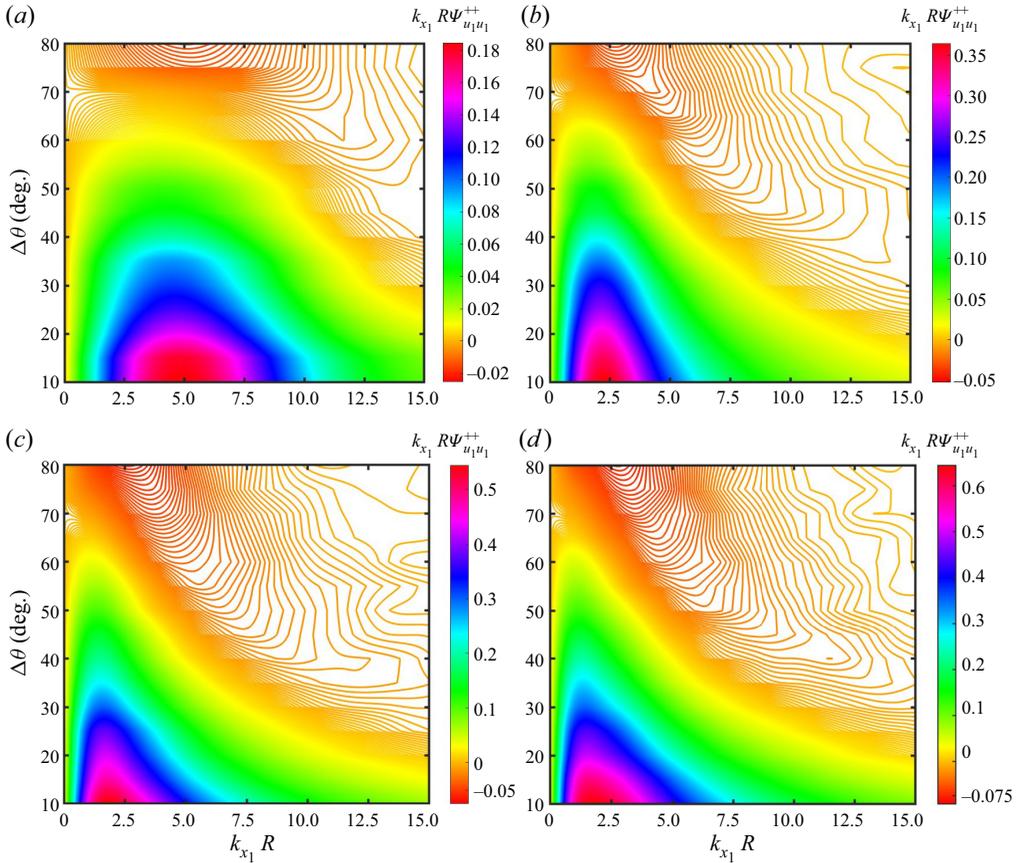
Figure 13. Isocontours of $k_{x_1}R\Psi_{u_1u_1}^{++}$ at fixed wall-normal location $x_2/R = 0.7$ and four Reynolds numbers: (a) $Re_\tau = 4100$, (b) $Re_\tau = 7700$, (c) $Re_\tau = 11\,500$, and (d) $Re_\tau = 15\,300$.

$k_{x_1}R\Psi_{u_1u_1}^{++}$ shown in both figures 13 and 14 emphasize the contribution of the LSMs to the azimuthal coherent structure. One thus could deduce from figures 11–14 clear evidence for the dependence of the cross-power spectral density and consequently the azimuthal pipe flow structure on the Reynolds number, the wall-normal location for various azimuthal separations.

In figures 11–14, at each azimuthal separation within the range $10° \leq \Delta\theta \leq 70°$, positive and negative values for $k_{x_1}R\Psi_{u_1u_1}^{++}$ were obtained – however, along different ranges of the streamwise wavenumber $k_{x_1}R$. To investigate further the effect of changing the azimuthal separation $\Delta\theta$, the wall-normal location x_2/R and the Reynolds number Re_τ on $k_{x_1}R\Psi_{u_1u_1}^{++}$, figure 15 was produced. Figure 15 consists of four plots. Figure 15(a) is a zoomed version of figure 12(d) to highlight the positive–negative/peak–trough values of $k_{x_1}R\Psi_{u_1u_1}^{++}$ versus $k_{x_1}R$ at $x_2/R = 0.7$ for azimuthal separations $10° \leq \Delta\theta \leq 210°$ and $Re_\tau = 4100$. Furthermore, each plot in figures 12(a)–(c) is zoomed and treated in a similar manner to the zoomed version of figure 12(d), and the outcomes, i.e. both peak/positive and trough/negative values of $k_{x_1}R\Psi_{u_1u_1}^{++}$, for all wall-normal locations $0.1 \leq x_2/R \leq 0.7$ and $Re_\tau = 4100$, are presented in figures 15(b,c). The effect of the wall-normal location x_2/R on either the peak/positive and trough/negative values of

973 A1-20
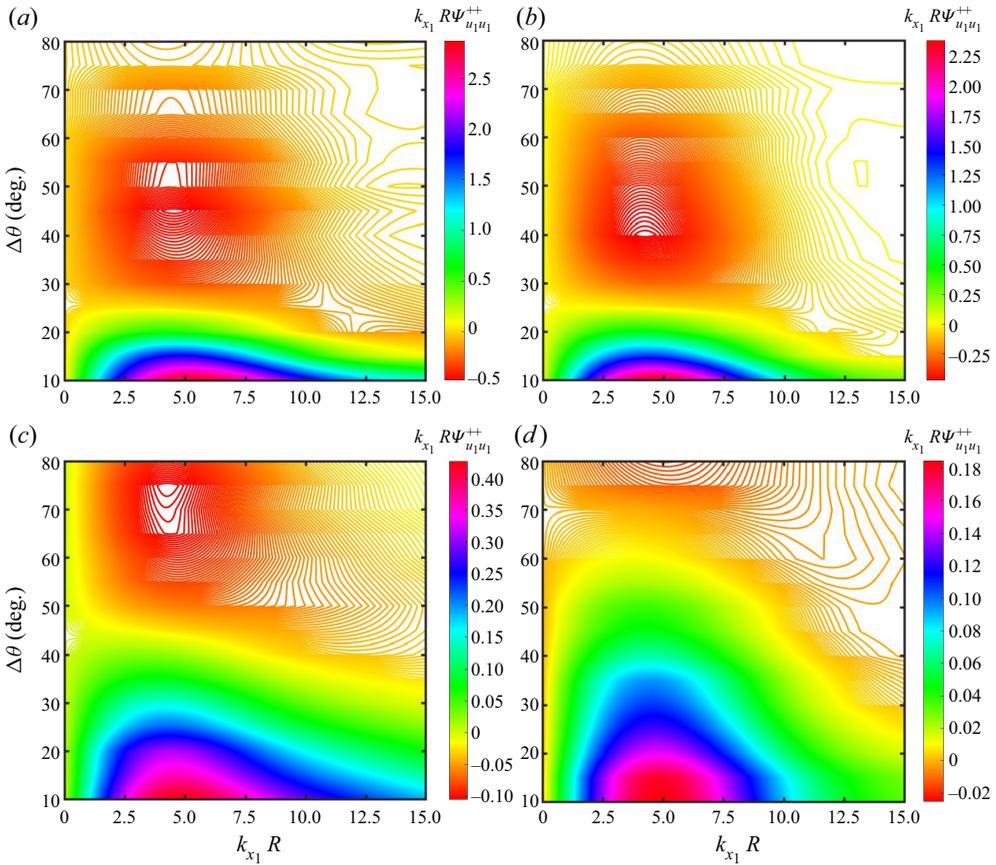
Figure 14. Isocontours of the real component of premultiplied cross-spectral density $k_{x_1} R \Psi_{u_1 u_1}^{++}$ at four wall-normal locations for Reynolds number $Re_\tau = 4100$ and $10° \leq \Delta\theta \leq 80°$: (*a*) $x_2/R = 0.1$, (*b*) $x_2/R = 0.2$, (*c*) $x_2/R = 0.5$, and (*d*) $x_2/R = 0.7$.

$k_{x_1} R \Psi_{u_1 u_1}^{++}$ is observable in both figures 15(*b,c*) for the same Reynolds number. However, such peak/positive, trough/negative behaviour of $(k_{x_1} R \Psi_{u_1 u_1}^{++})_{peak-trough}$ is more prominent for the wall-normal locations $x_2/R \leq 0.1$ and $x_2/R \leq 0.2$, as figure 15(*b*) indicates. In figure 15(*c*), for similar azimuthal probe separation and constant Reynolds number, a strong effect for the wall-normal location on either the peak/positive or trough/negative values of $k_{x_1} R \Psi_{u_1 u_1}^{++}$ is observable, in particular for $x_2/R = 0.1$ and 0.2. On the other hand, the peak values of $k_{x_1} R \Psi_{u_1 u_1}^{++}$ attenuate fast on moving away from the pipe wall, as both figures 15(*b,c*) illustrate. One would also observe from figure 15(*c*) that along an azimuthal separation range $45° \leq \Delta\theta \leq 150°$, $k_{x_1} R \Psi_{u_1 u_1}^{++}$ shows almost zero values, indicating that the two hot-wire signals are uncorrelated along this azimuthal separation range. Additionally, figure 15(*d*) represents the effect of the Reynolds number within the range $4100 \leq Re_\tau \leq 15\,300$ on the peak–trough values of $k_{x_1} R \Psi_{u_1 u_1}^{++}$ at $x_2/R = 0.7$ fixed wall-normal location. The figure shows a clear effect for the Reynolds number on peak/positive and/or trough/negative values of $k_{x_1} R \Psi_{u_1 u_1}^{++}$ at similar azimuthal separation $\Delta\theta$. Therefore, one would conclude that figure 15 is clear evidence for the dependence of

973 A1-21
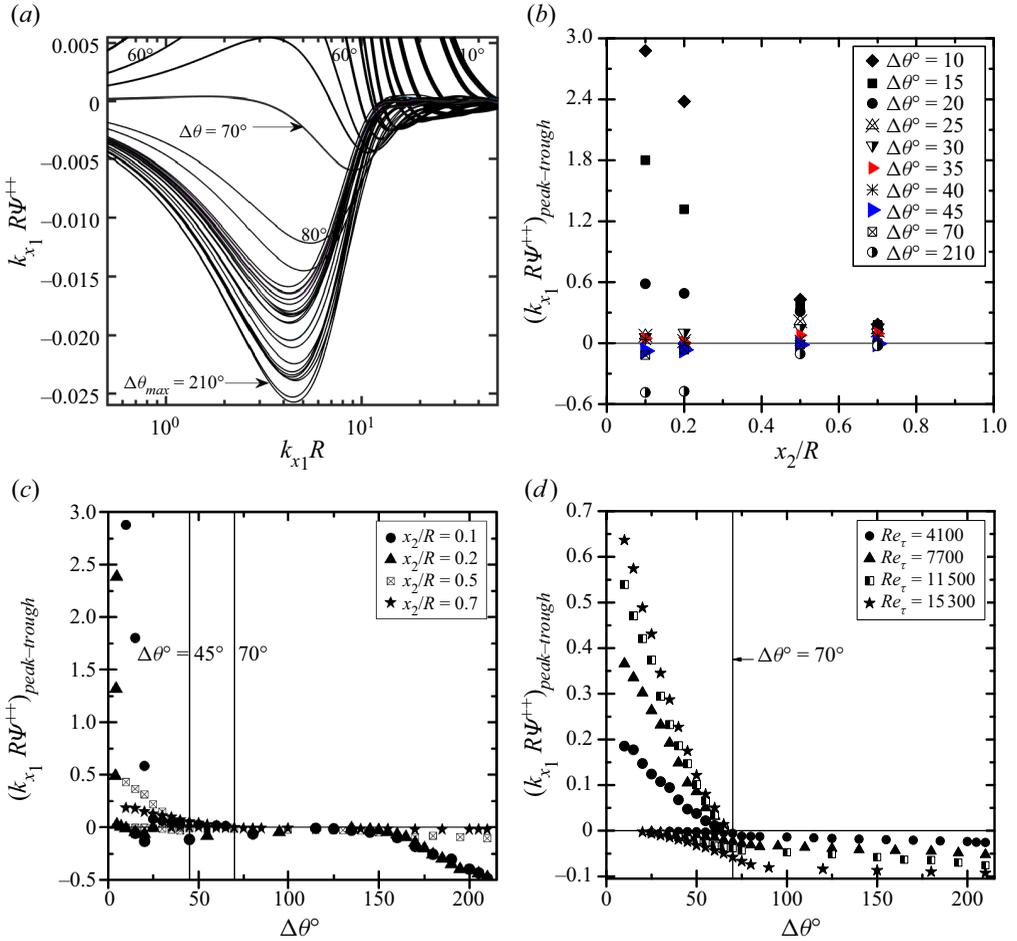
Figure 15. Peak–trough behaviour of the real component of premultiplied cross-power spectral density $k_{x_1} R \Psi_{u_1 u_1}^{++} = f(\Delta\theta, x_2/R, Re_\tau)$: (a) zoomed $k_{x_1} R \Psi_{u_1 u_1}^{++}$ versus $k_{x_1} R$; (b) $(k_{x_1} R \Psi_{u_1 u_1}^{++})_{peak-trough}$ versus x_2/R; (c) $(k_{x_1} R \Psi_{u_1 u_1}^{++})_{peak-trough}$ versus $\Delta\theta$ for $0.1 \leq x_2/R \leq 0.7$; (d) $(k_{x_1} R \Psi_{u_1 u_1}^{++})_{peak-trough}$ versus $\Delta\theta$ for $4.1 \times 10^3 \leq Re_\tau \leq 15.3 \times 10^3$. Plots are for (a) $Re_\tau = 4100$ and $x_2/R = 0.7$, (b) $Re_\tau = 4100$ and $10° \leq \Delta\theta \leq 210°$, (c) $Re_\tau = 4100$ and $0.1 \leq x_2/R \leq 0.7$, and (d) $4100 \leq Re_\tau \leq 15\,300$ and $x_2/R = 0.7$.

the azimuthal scale structure of the LSMs on the azimuthal separation $\Delta\theta$, the wall-normal location x_2/R and the Reynolds number Re_τ.

To assess quantitatively the fractional contribution of the large-scale motions, i.e. VLSM and LSM, to the azimuthal pipe flow structure, a spectral filtration for the cross-power spectral density was performed; see Bailey *et al.* (2008). The contribution of the VLSM was made via

$$\rho_{VL}(\Delta s, k_{x_1}) = \int_0^{(k_{x_1})_{cut}} \text{Re}[G(\Delta s, k_{x_1})] \, dk_{x_1}, \qquad (3.4)$$

where $(k_{x_1})_{cut}$ is the streamwise wavenumber corresponding to the first peak appearing in the premultiplied power spectra presented in both figures 7 and 8, and it depends on the wall-normal location and Reynolds number. Thus the contribution of the VLSMs to the pipe flow azimuthal structure was evaluated for $k_{x_1} \leq (k_{x_1})_{cut}$. On the other hand, the

973 A1-22

contribution of the LSMs is examined for $k_{x_1} \geq (k_{x_1})_{cut}$ using

$$\rho_L(\Delta s, k_{x_1}) = \int_{(k_{x_1})_{cut}}^{\infty} \text{Re}[G(\Delta s, k_{x_1})] \, dk_{x_1}. \tag{3.5}$$

The azimuthal distribution of both $\rho_{VL}(\Delta s, k_{x_1})$ and $\rho_L(\Delta s, k_{x_1})$ for $k_{x_1} \leq (k_{x_1})_{cut}$ and $k_{x_1} \geq (k_{x_1})_{cut}$, respectively, are presented in figure 16 for $0.1 \leq x_2/R \leq 0.7$ and $Re_\tau = 7700$, and compared to the azimuthal distribution of the streamwise velocity correlation $R_{u_1 u_1}(\Delta s)$. For similar Reynolds numbers, a clear dependence of both $\rho_{VL}(\Delta s, k_{x_1})$ and $\rho_L(\Delta s, k_{x_1})$ on the azimuthal separation Δs and the wall-normal location x_2 is observable. For small azimuthal separation $\Delta s/R \leq 1$, one would observe agreement with Bailey *et al.* (2008), but with the discernible difference that the magnitude of $\rho_{VL}(\Delta s, k_{x_1})$ is greater than that of $\rho_L(\Delta s, k_{x_1})$, reflecting an increased contribution of the VLSM to the azimuthal pipe flow structures. This observation is also a good indication that the azimuthal scales vary with the wall-normal location as well as with the azimuthal separation. Figure 16 stresses the effect of scale averaging when using (1.1) compared to the azimuthal scales estimated based on both (3.4) and (3.5), addressing the contributions of the large-scale motions, i.e. VLSM and LSM, respectively, as will be shown later, in figure 19. However, one might observe from figure 16 changes in the magnitude and ranges of the negative values of both $\rho_{VL}(\Delta s, k_{x_1})$ and $\rho_L(\Delta s, k_{x_1})$ versus the wall-normal distance for fixed Reynolds number. Referring to figure 7(*a*) for $x_2/R = 0.1$, where the VLSM is more energetic than the LSM, the VLSM contributes more to the azimuthal correlation coefficient, as figure 16(*a*) indicates. The contribution of the VLSM decreases, however, on moving away from the pipe wall, and on reaching $x_2/R = 0.5$, one would observe, as figure 7(*c*) indicated, that the energy contained in the LSM is larger relative to that contained in the VLSM, reflecting changes in the contribution of the LSM to the azimuthal correlation coefficient $\rho_L(\Delta s, k_{x_1})$ when compared to the contribution of the VLSM, as figure 16 illustrates.

3.4. *Coherence function*

To investigate further the behaviour of the azimuthal large scales at some specific wavenumbers in correspondence with the VLSM and LSM, the coherence function is introduced. It is a measure of the correlation between the two streamwise velocity fluctuating signals received from both probes, but in terms of the energy contained at specific wavenumbers. Bendat & Piersol (2000) introduced the so-called magnitude-squared coherence or the coherence function, defined as

$$\gamma^2(\Delta s, k_{x_1}) = \frac{|\Psi(\Delta s, k_{x_1})|^2}{\Phi(0, k_{x_1}) \, \Phi(\Delta s, k_{x_1})}. \tag{3.6}$$

This definition of the coherence function results in loss of its negative values, which have potential to assess the azimuthal scales of the coherent structures. Thus, in alignment with Bailey *et al.* (2008), we adopted the following definition of the coherence function:

$$\gamma(\Delta s, k_{x_1}) = \frac{\Psi(\Delta s, k_{x_1})}{\Phi^{1/2}(0, k_{x_1}) \, \Phi^{1/2}(\Delta s, k_{x_1})}, \tag{3.7}$$

quantifying the differences in the behaviour of the azimuthal scales as a result of the VLSM and LSM, where $\Psi(\Delta s, k_{x_1})$ as defined earlier is the real component of
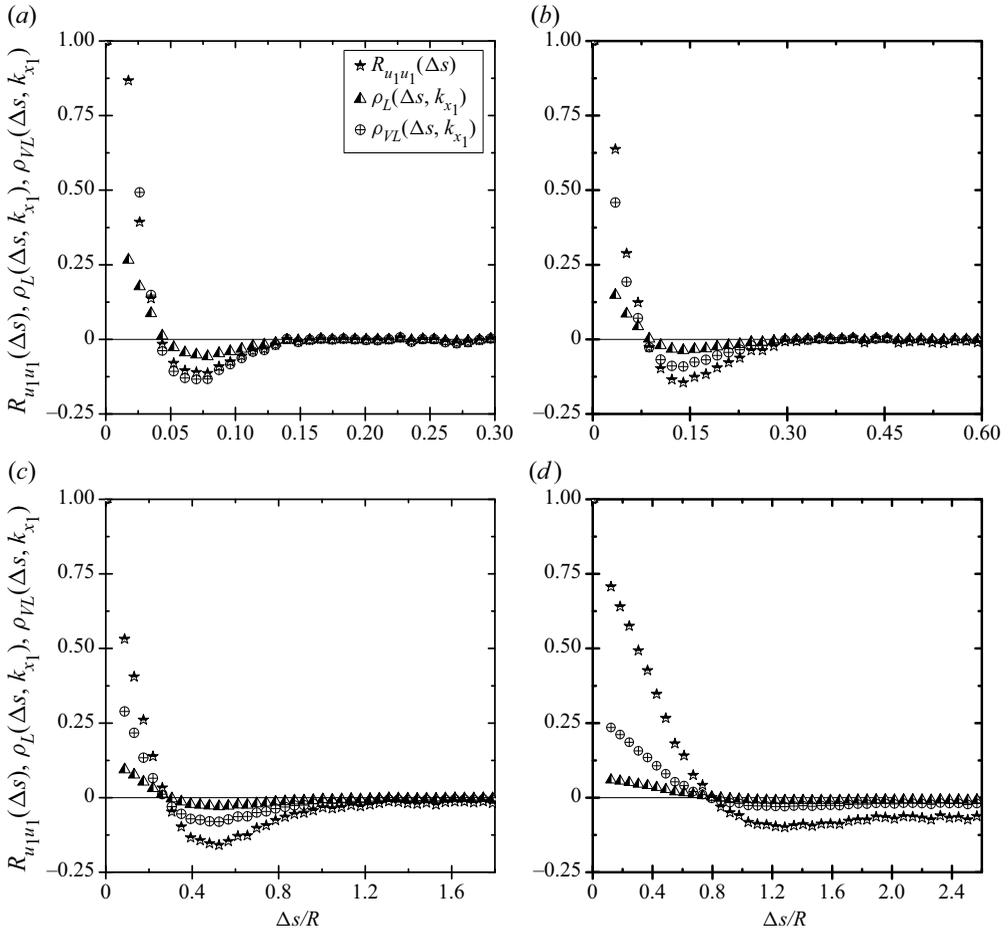
Figure 16. Azimuthal distributions of $\rho_{VL}(\Delta s, k_{x_1})$ and $\rho_L(\Delta s, k_{x_1})$ for (a) $x_2/R = 0.1$, (b) $x_2/R = 0.2$, (c) $x_2/R = 0.5$ and (d) $x_2/R = 0.7$, for Reynolds number $Re_\tau = 7700$.

the cross-power spectral density $G(\Delta s, k_{x_1})$, $\Phi(0, k_{x_1})$ is the auto-spectral density of the streamwise velocity fluctuations received from the fixed radial hot-wire probe, and $\Phi(\Delta s, k_{x_1})$ is the auto-spectral density of the streamwise velocity fluctuations measured by the traversing azimuthal probe.

It was shown earlier in power spectra presented in both figures 7 and 8 that two specific wavenumbers related to the VLSMs and LSMs were determined. Hence the coherence function $\gamma(\Delta s, k_{x_1})$ should be computed at such corresponding wavenumbers. In spite of the fact that the coherence function and the spectral density functions are pairs of the Fourier transform, the coherence function is more convenient for evaluating the azimuthal scales of the LSMs; see Bailey *et al.* (2008) and Bendat & Piersol (2000). Figure 17 represents the azimuthal distribution of $\gamma(\Delta s, k_{x_1})$ estimated at the streamwise wavenumbers corresponding to both the VLSM and the LSM at four wall-normal locations for $Re_\tau = 4100$. At first glance, one concludes that the distribution of $\gamma(\Delta s, k_{x_1})$ is similar to those of $R_{u_1u_1}(\Delta s)$ shown earlier in both figures 9 and 10. It is observable from figure 17, however, that at the same azimuthal separation $\Delta s/R$, the magnitude of $\gamma(\Delta s, k_{x_1})$ has higher negative values than those for $R_{u_1u_1}(\Delta s)$, reflecting the effect of the ensemble averaging of the various scales of flow motions introduced in the traditional definition of

973 A1-24
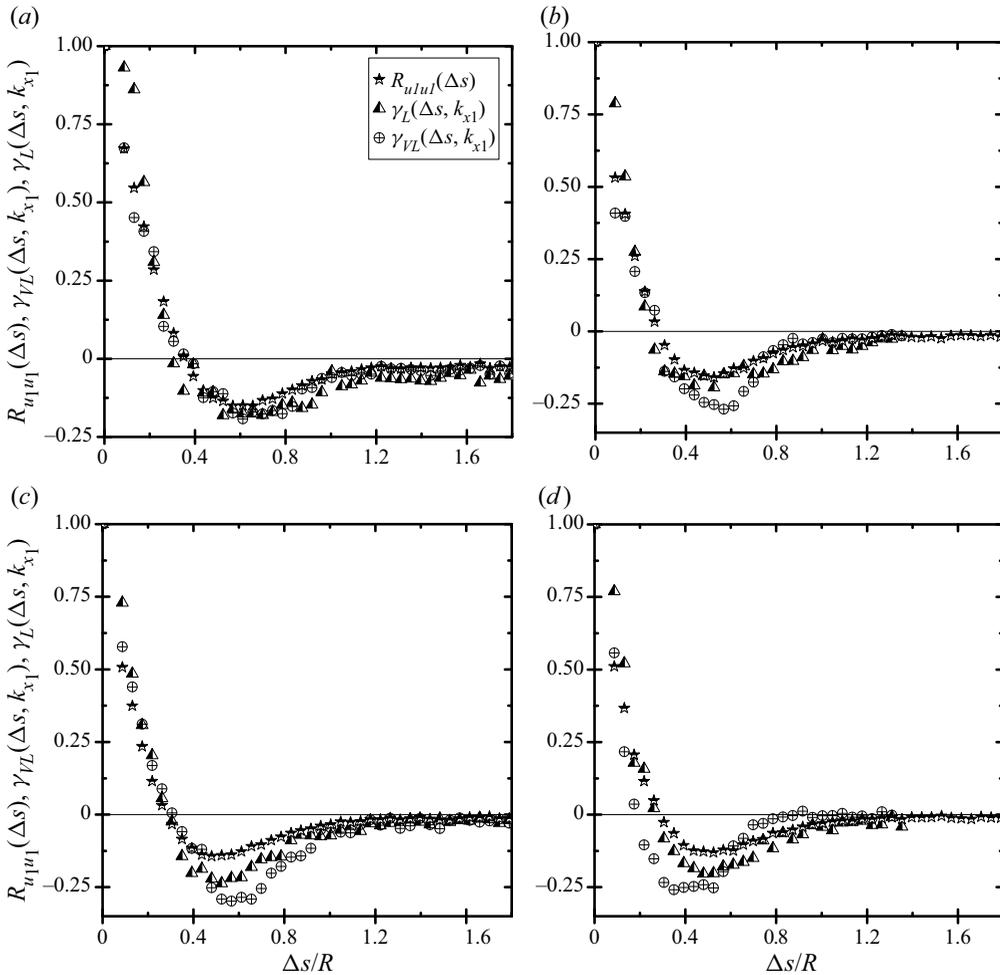
Figure 17. Azimuthal coherence function $\gamma(\Delta s, k_{x_1})$ based on streamwise wavenumbers corresponding to LSMs and VLSMs at four wall-normal locations for Reynolds number $Re_\tau = 4100$: (*a*) $x_2/R = 0.1$, (*b*) $x_2/R = 0.2$, (*c*) $x_2/R = 0.5$, and (*d*) $x_2/R = 0.7$.

the streamwise velocity correlation $R_{u_1u_1}(\Delta s)$. On the contrary, the effect of the averaging in $\gamma(\Delta s, k_{x_1})$ is limited to two main wavelengths corresponding to the two-mode peaks observed in both figures 7 and 8 identifying the VLSM and LSMs.

To quantify the azimuthal length scale (ℓ_z^+) of the LSMs, selected samples of the streamwise velocity correlation $R_{u_1u_1}(\Delta s)$ for $Re_\tau = 4100$ and 7700 are presented versus the azimuthal probe separation in wall units Δs^+ in figure 18, where $\Delta s^+ = \Delta s\, u_\tau/\nu$. The $R_{u_1u_1}(\Delta s)$ correlation drops from 1 to negative values at a range of azimuthal displacement $\Delta s^+ \approx 100$–5500 wall units, depending on the Reynolds number. Both plots in figure 18 show a similar trend where the value of $R_{u_1u_1}(\Delta s)$ drops to negative values, indicating the occurrence of alternating high-speed and low-speed regions of velocity fluctuations in the azimuthal direction. A threshold 0.05 is proposed in figure 18 to estimate the azimuthal length scale (ℓ_z^+) of the LSMs based on $R_{u_1u_1}(\Delta s)$. In a similar manner, the azimuthal length scale is thus computed across the whole range of the wall-normal locations, i.e. $0.1 \le x_2/R \le 0.7$, and Reynolds numbers $4100 \le Re_\tau \le 15\,300$, and the
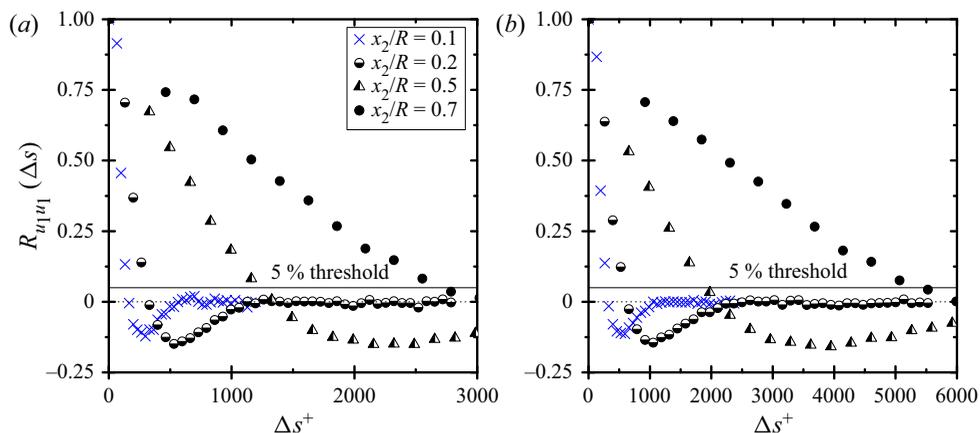
Figure 18. The azimuthal velocity correlation $R_{u_1 u_1}(\Delta s)$ of the streamwise velocity fluctuations at four wall-normal locations $0.1 \le x_2/R \le 0.7$ versus the azimuthal displacement in wall units Δs^+: (*a*) $Re_\tau = 4100$, (*b*) $Re_\tau = 7700$.

results are illustrated in figures 19(*a*,*b*). The results indicate that typical azimuthal scales of the large flow structures increase in diameter with increase in the wall-normal distance, in qualitative agreement with a similar observation made by Ganapathisubramani *et al.* (2005) for flat-plate boundary layer flow. The figure shows linear behaviour of the azimuthal growth of the large-scale structures across the logarithmic layer, in close agreement with Tomkins & Adrian (2003), Monty *et al.* (2007) and Bailey *et al.* (2008). On the other hand, a nonlinear increase versus the wall distance through the core region, i.e. $x_2/R \ge 0.5$, is remarkable. Focusing more on the ℓ_z/R data trend in figure 19(*a*), it does indeed appear nonlinear/concave-up, whereas in figure 9(*a*) of Bailey *et al.* (2008), the ℓ_z/δ results from a couple of experiments seem quite linear, modestly far from the wall – however, overall concave-down. It is worth noting here that most of the earlier azimuthal studies did not cover either the core region of the pipe flow or the outer region of the boundary layer, thus the nonlinear behaviour of the azimuthal structure was not discovered. For instance, using high spatial resolution particle image velocimetry, Tomkins & Adrian (2003) reported that several spanwise length scales vary, remarkably, linearly along the logarithmic layer in support of the attached-eddy hypothesis (Townsend 1956). Note that measurements of Tomkins & Adrian (2003) were limited to the wall-normal distances $x_2/\delta \le 0.2$. The discrepancy observed between the present finding versus the literature might be attributed partially to unequal ranges of the wall-normal distances and the Reynolds numbers. The uncertainty in calibration equations and spatial resolutions of the hot-wire probes to resolve small-scale turbulent fluctuations also has to be taken into consideration.

Moreover, Bailey *et al.* (2008) claimed that the azimuthal length scale ℓ_z variation versus the wall-normal location x_2 is completely linear when scaled appropriately by the local circumference $(2\pi r)$ at a given height to account for the pipe geometry. Note that the Bailey *et al.* (2008) data were limited to the wall-normal distances $0.1 \le x_2/R \le 0.5$. The current pipe data for $0.1 \le x_2/R \le 0.7$ are examined in a similar manner to Bailey *et al.* (2008) and plotted in figure 19(*b*). The present $\ell_z/(2\pi r)$ data showed very strong deviation from linearity in the core region of the pipe, i.e. for the final measurement location at $x_2/R = 0.7$, in which case this would constitute a significant deviation from Tomkins &

973 A1-26
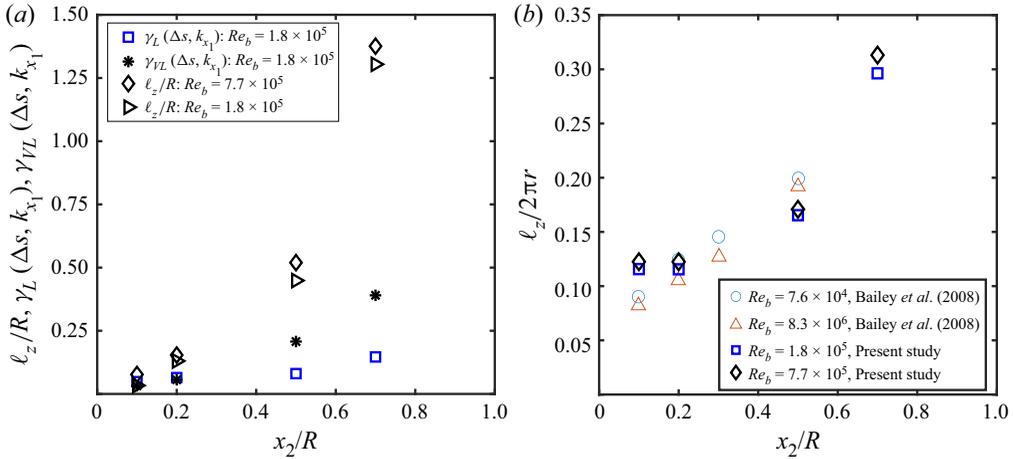
Figure 19. Normalized azimuthal length scale ℓ_z/R of azimuthal LSMs based on velocity correlations of the streamwise velocity fluctuations (*a*) compared to $\gamma_L(\Delta s, k_{x_1})$ and $\gamma_{VL}(\Delta s, k_{x_1})$ (present data), and (*b*) locally scaled by $2\pi r$ and compared to Bailey *et al.* (2008) ($Re_b = 7.6 \times 10^4$ and 8.3×10^6).

Adrian (2003), Monty *et al.* (2007) and Bailey *et al.* (2008). Figure 19(*b*) might support the idea that the nonlinearity is not a result of the pipe geometry alone (Townsend 1956), as Bailey *et al.* (2008) suggested. The nonlinear behaviour observed in the present study is beyond the top of the logarithmic layer, i.e. in the core region of the pipe where the attached-eddy hypothesis deviates. However, the significant difference in the wall-normal behaviours of the azimuthal scales of the observed LSM and VLSM is in alignment with a conclusion made by Bailey *et al.* (2008) that the LSM and VLSM are independent entities.

3.5. *Streamwise large-scale structure*

Intensive efforts have been recognized – see e.g. Theodorsen (1952), Townsend (1956), Grant (1958), Lumley (1967), Sabot *et al.* (1973), Cantwell (1981), Hussain (1983, 1986), Robinson (1991), Wark & Nagib (1991), Kim & Adrian (1999), Tomkins & Adrian (2003), Morrison (2007), Monty *et al.* (2007), Marusic *et al.* (2010), Smits *et al.* (2011*b*), Chung *et al.* (2015), Baidya *et al.* (2019) and Zanoun *et al.* (2019) – addressing questions often raised in the literature concerning the large-scale structures in wall-bounded shear flows. Nevertheless, a concrete definition of the origin, nature and time evolution of such structures is still under debate (see e.g. Marusic *et al.* 2010; Jiménez 2018), motivating further investigations to characterize, appropriately, the large-scale structures, in particular at high Reynolds numbers. For instance, a number of scenarios have been proposed by Panton (2001), characterizing mechanisms for the sustenance of wall turbulence which related to the turbulence structures of wall-bounded shear flows. They have been classified recently by Marusic *et al.* (2010) into two broad classes: one class is based on instability and transient growth mechanisms principally in the inner region, and the other is based on vortex-structure regeneration mechanisms. In alignment with the view of Marusic *et al.* (2010), Del Álamo & Jiménez (2006) suggested that the LSMs might arise from nonlinear instabilities in pipe flow turbulence. However, the interpretation of the LSMs in most earlier studies agreed with the hairpin vortex paradigm of Theodorsen (1952). Thus the hairpin concept might be considered a universal element or a building block

of the large-scale structure of turbulent flow as proposed by Theodorsen (1952) and later adopted by Kim & Adrian (1999) and Adrian (2007). And adopting the conceptual model by Kim & Adrian (1999), the very-large-scale structure was defined as a consequence of coherence in the pattern of hairpin packets, i.e. the hairpin eddies that align coherently in groups to form long packets, and then packets align coherently to form the VLSMs.

In the present work, to highlight the sizes of the LSMs in the streamwise direction, intensive measurements using a single hot-wire probe were carried out, covering the inner and core regions of the pipe, i.e. $0.04 \leq x_2/R \leq 1$, through multiple radial locations. The analysis of the spectra shown earlier in both figures 7 and 8 proposed two-mode structures, i.e. a low-wavenumber mode and a moderate-wavenumber mode.

Further data analysis was therefore carried out, allowing estimations of the streamwise sizes of the large-scale structures, and the outcome is presented in figure 20. Figure 20 illustrates for different Reynolds numbers the values of the wavelengths λ_{max}/R of the two-mode flow structures versus the wall-normal location x_2/R, both normalized by the pipe radius R. Although the validity of Taylor's hypothesis to convert temporal hot-wire signals into spatial domain data remains a big concern (see e.g. Zaman & Hussain 1981; Marusic *et al.* 2010), it was used in the present study to estimate the sizes of the streamwise large-scale structures. Thus, based on similar analysis for the spectral peaks observed in figures 7 and 8, the sizes of the large-scale structures were estimated using the Taylor hypothesis discussed in § 3.1, and the results are presented in figure 20. Briefly, the indices/wavenumbers at which the first and second local maxima/peaks of the energy spectra occur are determined in correspondence with the VLSMs and LSMs, respectively. Thereafter, the wavelengths $\lambda_{x_1} = 2\pi/k_{x_1}$ associated with the low and moderate wavenumbers for the very-large-scale and large-scale structures were estimated and then normalized with the pipe radius λ_{x_1}/R, respectively. In figure 20, it is observed that the wavelengths of those structures change significantly along the pipe wall-normal distance as well as with the Reynolds number. Figure 20(*a*) is a semi-logarithmic representation of the large-scale structures. Thus one might observe slight differences between the LSMs and VLSMs within the buffer layer. The figure illustrates also that the very-large-scale structures start roughly at the top of the buffer layer, in agreement with a similar conclusion made by Kim & Adrian (1999), and grow rapidly in wavelength λ_{x_1} through the logarithmic region, reaching maximum wavelengths $\lambda_x \approx 12R$, $\lambda_x \approx 16R$ and $\lambda_{x_1} \approx 18R$ for $Re_\tau = 3200$, $Re_\tau = 11\,000$ nd $Re_\tau \approx 16\,000$, respectively, at approximately half of the pipe radius $x_2/R \approx 0.5$, i.e. outside the logarithmic layer. A sudden drop in the wavelength of the VLSM occurs at $x_2/R \approx 0.5$, which is also in alignment with an observation made by Meinhart & Adrian (1995) and Kim & Adrian (1999) that the VLSMs are associated with the zones of uniform low momentum found in the boundary layer, which extend only up to approximately one-half of the boundary layer thickness or the pipe radius. Figure 20(*b*) is a linear plot, better showing the LSM along the core region of the pipe. One structure beyond $x_2/R = 0.5$, having wavelength $\lambda_x \approx 3R$, is observable. Hence one concludes from figures 20(*a,b*) that the LSM spans the pipe cross-section from a location close to the pipe wall, i.e. within the buffer layer, to the centreline of the pipe, having wavelength λ_x around $3R$ in plausible agreement also with Kim & Adrian (1999). The constant behaviour of the LSM along the buffer and the logarithmic layers might be attributed to the attached-eddy model of wall turbulence; see e.g. Marusic & Monty (2019).
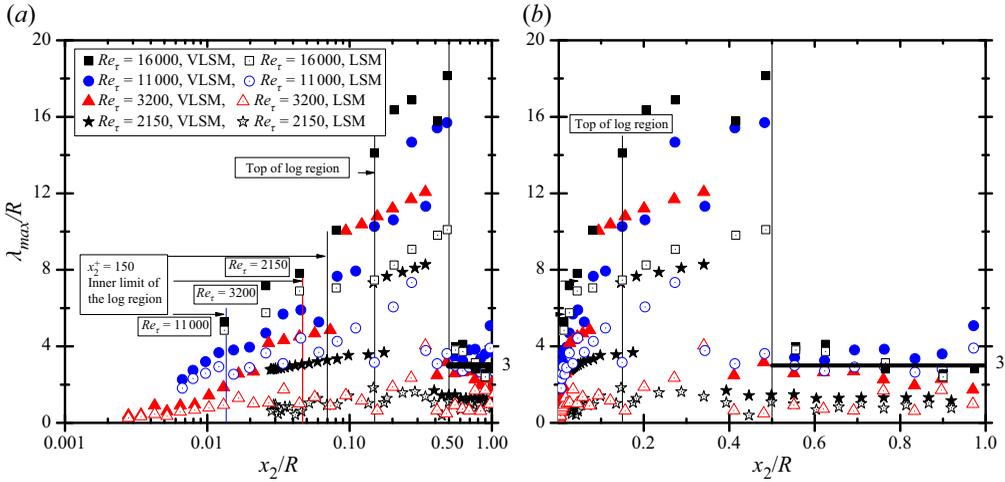
Figure 20. (*a*) Semi-logarithmic and (*b*) linear representations of the dimensionless wavelengths of the LSMs and VLSMs versus the normalized wall-normal distances for $2150 \leq Re_\tau \leq 16 \times 10^3$.

4. Discussions and conclusions

Experimental studies identifying the growth mechanisms of the azimuthal and/or spanwise flow scales are scarce, motivating the present work. To shed some light on the azimuthal scales of the pipe flow, experimental data for the streamwise velocity component have been documented in light of two-point joint statistics and spectral analysis at a pipe location where flow was assured to be fully developed for shear Reynolds number in the range $2 \times 10^3 \leq Re_\tau \leq 16 \times 10^3$. The streamwise velocity fluctuations were measured at two equal radial locations simultaneously, within $0.1 \leq x_2/R \leq 0.7$, for various azimuthal probe separations, utilizing two single hot-wire probes. Precise *in situ* calibration was adopted with least-squares errors better than $\pm 1\%$ for both hot-wire probes. The blockage of the pipe cross-section due to probe holders during calibration and measurements ranged from 0.4 % to 2.8 % for wall-normal locations $x_2/R = 0.1$ and $x_2/R = 0.7$, respectively. The streamwise velocity component was measured with uncertainty within the ranges $\pm 0.4\%$ to $\pm 1.6\%$ and $\pm 0.7\%$ to $\pm 2.67\%$ in the local mean velocity and the turbulence intensity level, respectively, obtained from either the fixed or the movable azimuthal hot-wire probes.

The physical mechanism of azimuthal growing of the LSMs throughout the logarithmic layer and core region shown in figure 19 can be explained well using earlier attempts made to quantify the growth of the azimuthal scales via streaks merging on an eddy-by-eddy basis: splitting, increased spacing, or coalescence and divisions; see e.g. Nakagawa & Nezu (1981), Smith & Metzler (1983) and Wark & Nagib (1991). Recent measurements by Adrian, Meinhart & Tomkins (2000) revealed also a degree of vortex organization in the logarithmic layer, supporting the data in figure 19. In addition, Tomkins & Adrian (2003) extended, experimentally, the vortex packet model in similarity to the Λ vortex growth model of Perry & Chong (1982), observing that the structure becomes dependent on the distance from the wall at elevated Reynolds number. It was also observed by Monty *et al.* (2007) that the hairpin structures project into the pipe flow core region, however, resulting in azimuthally large hairpin packets within it, verifying data presented in figure 19. The large spanwise scales were also shown to be related to the large streamwise scales, on average, providing a link to the results of Wark & Nagib (1991),

interpreting the growth of the azimuthal turbulent flow structures versus the wall-normal distance Hutchins & Marusic (2007) and Monty *et al.* (2007). Thus as the alignment of the large scale is believed to be the source of the VLSM, the resulting VLSM imposed within the logarithmic layer can be expected to be of wider scale, supporting the present findings.

Further, to conclude, using energy spectra, azimuthal two-point velocity correlation and cross-power spectral density, the present experimental data were evaluated, resulting in the following.

(i) Two discernible peaks in energy spectra were observed: one at a low streamwise wavenumber associated with the very-large-scale motion (VLSM), and the second at moderate streamwise wavenumber associated with the large-scale motion (LSM). The two observable peaks in the energy spectra obtained are clear evidences or footprints for the LSMs in the pipe flow. Both peaks decrease in energy content with increase in the wall-normal distance; however, the energy contained in the VLSM peak decreases faster than that for the LSM for $x_2/R < 0.5$. It was observed that the LSM peak at $x_2/R \geq 0.5$ is more prominent than the VLSM peak, which disappeared for wall-normal locations $x_2/R > 0.5$. The physical model proposed by Meinhart & Adrian (1995) and Kim & Adrian (1999) is appropriate to interpret the disappearance of the VLSM peak beyond $x_2/R = 0.5$, as discussed earlier. Clear dependence of the magnitude of the energy peaks at the corresponding wavenumbers for the VLSM and the LSM on both the wall-normal location and the Reynolds number was observable.

(ii) The two-point velocity correlation coefficient $R_{u_1 u_1}(\Delta s)$ was discussed, revealing a clear effect for the wall-normal location, the azimuthal separation; however, the weak Reynolds number effect on the azimuthal pipe flow structure was not addressed earlier in the literature. The positive–negative trends of the correlation coefficient obtained represent an indication of the vortex-packets/hairpin pipe flow structure, in agreement with similar observations made by Tomkins & Adrian (2003) and Monty *et al.* (2007) for flat-plate boundary layer and pipe flows, respectively.

(iii) Appropriate contributions of the LSMs to the azimuthal pipe flow structures were treated using the cross-power spectral density as a function of the wall-normal location, the azimuthal separation and the Reynolds number. The real part of the cross-power spectral density normalized $k_{x_1} R \Psi_{u_1 u_1}^{++}$ as a function of the azimuthal separation and the streamwise wavenumber, indicating a peak–trough mode for various wall-normal locations and Reynolds numbers. The peak was observed to attenuate rapidly for wall-normal locations $x_2/R \leq 0.2$, and in particular for azimuthal separation $\Delta \theta \leq 45°$. Such rapid decay observed in $k_{x_1} R \Psi_{u_1 u_1}^{++}$ might be interpreted by the hairpin vortex model proposed by Theodorsen (1952). On the contrary, for the wall-normal locations $x_2/R > 0.2$, $k_{x_1} R \Psi_{u_1 u_1}^{++}$ showed slow rate of decay versus the azimuthal separation $\Delta \theta$, which could be attributed to the relatively long lifetimes of the azimuthal vortices found predominantly in the pipe core region. A clear dependence of the cross-power spectral density and consequently the azimuthal-scale structure of the LSMs on the azimuthal separation $\Delta \theta$, the wall-normal location x_2/R and the Reynolds number Re_τ was emphasized.

(iv) Spectral filtration for the cross-power spectral density was discussed, addressing well the energetic contribution of the large-scale motions, i.e. VLSM and LSM, to the azimuthal pipe flow structures. The contribution of the LSMs was observed to change on moving away from the pipe wall, indicating that the azimuthal scales vary with the wall-normal location as well as with the azimuthal separation for similar Reynolds numbers.

(v) The coherence function was discussed to address the behaviour of the azimuthal structure due to the LSMs. The azimuthal scales were identified in correspondence with wavenumbers that have been associated with the two-mode peaks observed in the energy spectra of the streamwise velocity fluctuations. They were computed along the four wall-normal locations $0.1 \leq x_2/R \leq 0.7$, showing sizes in the range $0.1 \leq \ell_z^+ \leq 0.5R$. The azimuthal scales increase in diameter with increase in the wall-normal distance, in qualitative agreement with a similar observation made by Ganapathisubramani *et al.* (2005) for flat-plate boundary layer flow. A linear increase in the azimuthal length scale through the log region was obtained, in plausible agreement with Tomkins & Adrian (2003), Monty *et al.* (2007) and Bailey *et al.* (2008). On the other hand, considering the wall-normal locations $0.1 \leq x_2/R \leq 0.7$, a nonlinear increase in azimuthal scales versus the wall distance was remarkable in the core region of the pipe. The nonlinearity behaviour observed is beyond the top of the log layer, i.e. in the core region of the pipe where the attached-eddy hypothesis deviates, constituting also a significant deviation from experimental data in the literature, e.g. Ganapathisubramani *et al.* (2005), Monty *et al.* (2007) and Bailey *et al.* (2008). The azimuthal scales of both the VLSM and LSM provided a basis proposing that the large-scale structures are independent entities in alignment with Bailey *et al.* (2008), and supporting the possibility that such large structures arise from linear and/or nonlinear models within the turbulent flow; see Jiménez, Del Álamo & Flores (2004) and Del Álamo & Jiménez (2006).

(vi) Additionally, the streamwise scales of the LSMs were identified using the auto-spectral energy analysis in correspondence with wavenumbers associated with the two-mode peaks observed in the energy spectra of the streamwise velocity fluctuations. The streamwise VLSMs and LSMs showed wavelengths $\approx 18R$ and $\approx 3R$, for $Re_\tau \approx 16 \times 10^3$ at half of the pipe radius, respectively. The streamwise large-scale structure, however, spans from the buffer layer to the centreline of the pipe, partially in alignment with the wall-attached-eddy concept.

To summarize, the present experiments emphasize clear dependence of the azimuthal scales on the Reynolds number and the azimuthal separation, as well as on the wall-normal location, that has not been reported previously. The present results in the pipe core/outer region disagree with experiments in the literature, none of which showed a nonlinear increase in azimuthal and/or spanwise length scales with increasing wall-normal distance. The streamwise LSMs were addressed, showing also clear dependence on both the wall-normal locations and the Reynolds number.

Author ORCIDs.
Ⓓ E.-S. Zanoun https://orcid.org/0000-0003-3834-1348.

Appendix A. Uncertainty in energy spectra of the streamwise velocity fluctuations

It is evident that precise measurement of higher-order streamwise velocity correlations requires calibrating hot-wire probes in potential flows with a large number of independent

data points. The streamwise instantaneous velocity component $\hat{U}_1$ can be written as

$$\hat{U}_1 = \bar{U}_1 + u_1, \tag{A1}$$

where $\bar{U}_1$ is the ensemble-averaged streamwise velocity, and u_1 represents the streamwise velocity fluctuation. The instantaneous hot-wire output $\hat{E}$ can be also written as

$$\hat{E} = \bar{E} + e', \tag{A2}$$

where $\bar{E}$ is the average hot-wire voltage output, and e' represents fluctuations in hot-wire output; both are due to the streamwise velocity component. The instantaneous hot-wire output $\hat{E}$ is related to the instantaneous streamwise velocity component $\hat{U}_1$ based on the power-law calibration function as follows:

$$\hat{E}^2 = A + B\hat{U}_1^n \quad \Rightarrow \quad \text{time averaging} + \text{low fluctuations} \quad \Rightarrow \quad \bar{E}^2 = A + B\bar{U}_1^n, \tag{A3}$$

where A, B and n are constants. Using the Taylor series expansion, the hot-wire output $\hat{E}(\hat{U}_1)$ can be expanded around the mean of the streamwise velocity component $\bar{U}_1$ as

$$\hat{E}(\hat{U}_1) = \bar{E}(\bar{U}_1) + \left[\frac{\partial \hat{E}(\hat{U}_1)}{\partial \hat{U}_1}\right]_{\hat{U}_1 = \bar{U}_1} (\hat{U}_1 - \bar{U}_1) + \text{HOT}. \tag{A4}$$

The constant temperature anemometer features significant nonlinearity that might require considering higher-order terms (HOT) in the Taylor series expansion. However, for the sake of simplicity, neglecting the HOT results in

$$\hat{E}(\hat{U}_1) - \bar{E}(\bar{U}_1) \approx \left[\frac{\partial \hat{E}}{\partial \hat{U}}\right]_{\hat{U} = \bar{U}_1} (\hat{U}_1 - \bar{U}) \quad \Rightarrow \quad e' \approx \left[\frac{\partial \hat{E}}{\partial \hat{U}}\right]_{\hat{U} = \bar{U}_1} u_1. \tag{A5}$$

Differentiating (A3) results in

$$\left[\frac{\partial \hat{E}}{\partial \hat{U}_1}\right]_{\hat{U}_1 = \bar{U}_1} = \frac{nB\bar{U}_1^{n-1}}{2\bar{E}}. \tag{A6}$$

Substituting (A6) into (A5) and rearranging results in the streamwise turbulence intensity

$$\frac{u_1}{\bar{U}_1} = \left[\frac{2\bar{E}}{n(\bar{E}^2 - A)}\right] e'. \tag{A7}$$

The vigour/intensity of turbulence is usually evaluated via velocity fluctuations u_1. Moreover, errors in estimating the mean values of the streamwise velocity $\bar{U}_1$ and hot-wire output $\bar{E}$ are negligible compared to the error in measuring hot-wire fluctuations e'. Thus one can write the turbulent kinetic energy or energy spectra $u_1 u_1$ of the streamwise velocity fluctuations as

$$u_1 u_1 = C e'^2, \tag{A8}$$

where $C = [2\bar{E}\bar{U}_1/n(\bar{E}^2 - A)]^2$. To determine the sensitivity of the turbulent kinetic energy $u_1 u_1$ of the streamwise velocity fluctuations to any small perturbations/errors in

973 A1-32

Experiment parameter	Bailey *et al.* (2008)	Present study
Pipe diameter D	129.84 mm	190 ± 0.25 mm
Wall normal locations x_2/R	0.1, 0.2, 0.3, 0.5	0.1, 0.2, 0.5, 0.7
Reynolds number Re_τ	1.9×10^3–1.6×10^5	2×10^3–1.6×10^4
Blockage ratio %	Not reported	0.4–2.8 %
Viscous length scale $\ell_c[\mu]$	34–0.4	42–6
Probe length ℓ^+ wall units	14.6–1232	29–192
Calibration	Traditional *in situ*	Novel *in situ*
Calibration uncertainty	Not given	$\leq \pm 1\%$
Uncertainty in $u_1 u_1$	$\geq 10\%$	$\leq 2\%$
Roughness effects	Relatively insensitive to roughness	Hydraulically smooth
Dependence on x_2/R	Independent	Dependence is emphasized
Dependence on Reynolds number	Independent	Dependence is emphasized
Azimuthal correlation and structure	Little changes vs $x_2/R \geq 0.1$; however, independent of Re	Dependence on x_2/R is emphasized; dependence on Re is emphasized
Cross-spectra	Uncertainty $\geq \pm 10\%$	Uncertainty $\leq \pm 2\%$
Azimuthal scale ℓ_z	Decreases for $x_2/R \geq 0.2$; however, independent of x_2/R	Dependence on x_2/R is emphasized
Coherence function γ	Dependent on x_2/R for $x_2/R \leq 0.2$; however, independent of Re	Dependence on x_2/R is emphasized; dependence on Re is emphasized
Streamwise structures	Not treated	Treated

Table 3. A comparative summary, where $\ell^+ = \ell u_\tau / \nu$ is the hot-wire length in wall units, and ℓ_c is the viscous length scale.

hot-wire fluctuations $\epsilon_{e'}$ in (A8), the following notations were introduced to estimate how far the measured energy $u_1 u_1$ deviates from the true value:

$$u_1 u_1 = (u_1 u_1)^*(1 + \epsilon_{u_1 u_1}) \quad \text{and} \quad e'^2 = e'^{*2}(1 + \epsilon_{e'})^2, \qquad (A9a,b)$$

where ϵ refers to the perturbation or error in the measured quantity, while parameters with an asterisk indicate exact values. Introducing the notations used in (A9*a,b*) into (A8) results in

$$(u_1 u_1)^*(1 + \epsilon_{u_1 u_1}) = C e'^{*2}(1 + \epsilon_{e'})^2. \qquad (A10)$$

From (A8) and (A10), one can derive the following expression for the error estimation in the turbulent kinetic energy or the energy spectra:

$$(1 + \epsilon_{u_1 u_1}) = (1 + \epsilon_{e'})^2. \qquad (A11)$$

The partial derivatives of $\epsilon_{u_1 u_1}$ with respect to the perturbation parameter, $\epsilon_{e'}$ give

$$\frac{\partial \epsilon_{u_1 u_1}}{\partial \epsilon_{e'}} \approx 2(1 + \epsilon_{e'}). \qquad (A12)$$

This principal analysis indicates a direct linear relation between error introduced into the turbulent kinetic energy/energy spectra of the streamwise velocity fluctuations $u_1 u_1$ and error in fluctuating hot-wire output e'. Thus a $\pm 10\,\%$ calibration error or uncertainty results in $\approx \pm 20\,\%$ error in the turbulent energy spectra of the streamwise velocity fluctuations measured and consequently on scales of the turbulence structures.

Appendix B. Comparative summary

Due to some common similarities and differences between the present study and the earlier work done by Bailey *et al.* (2008), the authors present in table 3 a short comparison between the two studies.

REFERENCES

ADRIAN, R.J. 2007 Hairpin vortex organization in wall turbulence. *J. Phys. Fluids* **19**, 041301.
ADRIAN, R.J., MEINHART, C.D. & TOMKINS, C.D. 2000 Vortex organization in the outer region of the turbulent boundary layer. *J. Fluid Mech.* **422**, 1–54.
BAIDYA, R., *et al.* 2019 Simultaneous skin friction and velocity measurements in high Reynolds number pipe and boundary layer flows. *J. Fluid Mech.* **871**, 377–400.
BAILEY, S.C.C., HULTMARK, M., SMITS, A.J. & SCHULTZ, M.P. 2008 Azimuthal structure of turbulence in high Reynolds number pipe flow. *J. Fluid Mech.* **615**, 121–138.
BAILEY, S.C.C. & SMITS, A.J. 2010 Experimental investigation of the structure of large- and very-large-scale motions in turbulent pipe flow. *J. Fluid Mech.* **651**, 339–356.
BALAKUMAR, J. & ADRIAN, R.J. 2007 Large- and very-large-scale motions in channel and boundary-layer flows. *Proc. R. Soc. Lond.* A **365**, 665.
BENDAT, J.S. & PIERSOL, A.G. 2000 *Random Data: Analysis and Measurement Procedures*, 3rd edn. Wiley Interscience.
BLACKWELDER, R.F. 1988 Coherent structures associated with turbulent transport. In *Transport Phenomena in Turbulent Flows* (ed. M. Hirata & N. Kasagi), pp. 69–88. Hemisphere.
BLACKWELDER, R.F. & HARITONIDIS, J.H. 1983 Scaling of the bursting frequency in turbulent boundary layers. *J. Fluid Mech.* **132**, 87–103.
BOUFIDI, E., LAVAGNOLI, S. & FONTANETO, F. 2020 A probabilistic uncertainty estimation method for turbulence parameters measured by hot-wire anemometry in short-duration wind tunnels. *Trans. ASME J. Engng Gas Turbines Power* **142**, 031007.
BRUUN, H.H. 1995 *Hot-wire Anemometry*. Oxford University Press.

CANTWELL, J. 1981 Organised motion in turbulent flow. *Annu. Rev. Fluid Mech.* **148**, 457.

CHEN, J. 2019 Two-point statistics of coherent structure in turbulent flow. *J. Flow Control Meas. Vis.* **7**, 1–21.

CHUNG, D., MARUSIC, I., MONTY, J.P., VALLIKIVI, M. & SMITS, A.J. 2015 On the universality of inertial energy in the log layer of turbulent boundary layer and pipe flows. *Exp. Fluids* **56**, 141.

DEL ÁLAMO, J.C. & JIMÉNEZ, J. 2006 Linear energy amplification in turbulent channels. *J. Fluid Mech.* **55**, 205–213.

DURST, F., ZANOUN, E.-S. & PASHTRAPANSKA, M. 2001 In-situ calibration of hot wires close to highly heat-conducting walls. *J. Exp. Fluids* **31**, 103–110.

FIEDLER, H.E. 1988 Coherent structures in turbulent flows. *Prog. Aerosp. Sci.* **25**, 231–269.

GAD-EL-HAK, M. & BANDYOPADHYAY, P. 1994 Reynolds number effects in wall bounded turbulent flows. *Appl. Mech. Rev.* **47**, 307–365.

GANAPATHISUBRAMANI, B., HUTCHINS, N., HAMBLETON, W.T., LONGGMIRE, E.K. & MARUSIC, I. 2005 Investigation of large-scale coherence in a turbulent boundary layer using two-point correlations. *J. Fluid Mech.* **524**, 57–80.

GRANT, H.L. 1958 The large eddies of turbulent motion. *J. Fluid Mech.* **4**, 149–190.

HAN, J., HWANG, J., YOON, M., AHN, J. & SUNG, H.J. 2019 Azimuthal organization of large-scale motions in a turbulent minimal pipe flow. *J. Phys. Fluids* **31**, 055113.

HELLSTRÖM, L., SINHA, A. & SMITS, A.J. 2011 Visualizing the very-large-scale motions in turbulent pipe flow. *Phys. Fluids* **23**, 011703.

HINZE, J.O. 1975 *Turbulence*. McGraw-Hill.

HOLMES, P., LUMLEY, J.L., BERKOOZ, G., MATTINGLYA, J.C. & WITTENBERG, R.W. 1997 Low-dimensional models of coherent structures in turbulence. *Phys. Rep.* **287**, 337–384.

HOLMES, P., LUMLEY, J.L., BERKOOZ, G. & ROWLEY, C.W. 1996 *Turbulence, Coherent Structures, Dynamical Systems and Symmetry*. Cambridge University Press.

HUSSAIN, A.K.M.F. 1983 Coherent structures – reality and myth. *J. Phys. Fluids* **26**, 2816–2850.

HUSSAIN, A.K.M.F. 1986 Coherent structures and turbulence. *J. Fluid Mech.* **173**, 303–56.

HUTCHINS, N. & MARUSIC, I. 2007 Evidence of very long meandering features in the logarithmic region of turbulent boundary layers. *J. Fluid Mech.* **579**, 1–28.

HUTCHINS, N., MONTY, J.P. & HULTMARK, M. 2015 A direct measure of the frequency response of hot-wire anemometers: temporal resolution issues in wall-bounded turbulence. *Exp. Fluids* **56**, 18.

HUTCHINS, N., NICKELS, T.B., MARUSIC, I. & CHONG, M.S. 2009 Hot-wire spatial resolution issues in wall-bounded turbulence. *J. Fluid Mech.* **635**, 103–136.

JIMÉNEZ, J. 2018 Coherent structures in wall-bounded turbulence. *J. Fluid Mech.* **842**, P1.

JIMÉNEZ, J., DEL ÁLAMO, J.C. & FLORES, O. 2004 The large-scale dynamics of near-wall turbulence. *J. Fluid Mech.* **505**, 1795–1993.

JOVANOVIĆ, J. 2004 *The Statistical Dynamics of Turbulence*. Springer.

JOVANOVIĆ, J., YE, Q.-Y. & DURST, F. 1995 Statistical interpretation of the turbulent dissipation rate in wall-bounded flows. *J. Fluid Mech.* **293**, 321–347.

DE KAT, R. & GANAPATHISUBRAMANI, B. 2015 Frequency–wavenumber mapping in turbulent shear flows. *J. Fluid Mech.* **783**, 166–190.

KIM, C. & ADRIAN, R.J. 1999 Very large-scale motion in the outer layer. *J. Phys. Fluids* **11**, 417.

LIGRANI, P.M. & BRADSHAW, P. 1987 Subminiature hot-wire sensors: development and use. *J. Phys.* E **20**, 323–332.

LUMLEY, J.L. 1967 The structure of inhomogeneous turbulence. In *Atmospheric Turbulence and Wave Propagation* (ed. A.M. Yaglom & V.I. Tatarski), pp. 166–178. Nauka.

MARUSIC, I., MCKEON, B.J., MONKEWITZ, P.A., NAGIB, H.M., SMITS, A.J. & SREENIVASAN, K.R. 2010 Wall-bounded turbulent flows at high Reynolds numbers: recent advances and key issues. *J. Phys. Fluids* **22**, 065103.

MARUSIC, I. & MONTY, J.P. 2019 Attached eddy model of wall turbulence. *Annu. Rev. Fluid Mech.* **51**, 49–74.

MATHIS, R., HUTCHINS, N. & MARUSIC, I. 2009 Large-scale amplitude modulation of the small-scale structures in turbulent boundary layers. *J. Fluid Mech.* **628**, 311–337.

MEINHART, C.D. & ADRIAN, R.J. 1995 On the existence of uniform momentum zones in a turbulent boundary layer. *Phys. Fluids* **7**, 694.

MONIN, A.S. & YAGLOM, A.M. 1971 *Statistical Fluid Mechanics*. M.I.T. Press.

MONTY, J.P., STEWART, J.A., WILLIAMS, R.C. & CHONG, M.S. 2007 Large-scale features in turbulent pipe and channel flows. *J. Fluid Mech.* **589**, 147–156.

MORRISON, J.F. 2007 The interaction between inner and outer regions of turbulent wall-bounded flow. *Phil. Trans. R. Soc. Lond.* A **365**, 883.

MORRISON, J.F., MCKEON, B.J., JIANG, W. & SMITS, A.J. 2004 Scaling of the streamwise velocity component in turbulent pipe flow. *J. Fluid Mech.* **508**, 99–131.

NAKAGAWA, H. & NEZU, I. 1981 Structure of space–time correlations of bursting phenomena in an open-channel flow. *J. Fluid Mech.* **104**, 1–43.

OBERLACK, M. & PETERS, N. 1993 Closure of the two-point correlation equation in physical space as a basis for Reynolds stress models. In *Near-Wall Turbulent Flows* (ed. R.M.C. So, C.G. Speziale & B.E. Launder), pp. 85–94. Elsevier.

ÖRLÜ, R., FRANSSON, J.H.M. & ALFREDSSON, P.H. 2010 On near wall measurements of wall bounded flows – the necessity of an accurate determination of the wall position. *Prog. Aerosp. Sci.* **46**, 353–387.

PANTON, R.L. 2001 Overview of the self-sustaining mechanisms of wall turbulence. *Prog. Aerosp. Sci.* **37**, 341.

PERRY, A.E. & CHONG, M.S. 1982 On the mechanism of wall turbulence. *J. Fluid Mech.* **119**, 173–217.

ROBINSON, S.K. 1991 Coherent motions in the turbulent boundary layer. *Annu. Rev. Fluid Mech.* **23**, 601–639.

SABOT, J., RENAULT, J. & COMTE-BELLOT, G. 1973 Space–time correlations of the transverse velocity fluctuation in pipe flow. *Phys. Fluids* **16**, 1403–1405.

SMITH, C.R. & METZLER, S.P. 1983 The characteristics of low-speed streaks in the near-wall region of a turbulent boundary layer. *J. Fluid Mech.* **129**, 27–54.

SMITS, A.J., MCKEON, B.J. & MARUSIC, I. 2011a High-Reynolds number wall turbulence. *Annu. Rev. Fluid Mech.* **43**, 353–375.

SMITS, A.J., MONTY, J., HULTMARK, M., BAILEY, S.C.C., HUTCHINS, N. & MARUSIC, I. 2011b Spatial resolution correction for wall-bounded turbulence measurements. *J. Fluid Mech.* **676**, 41–53.

TALLURU, K.M., KULANDAIVELU, V. & HUTCHINS, N. 2014 A calibration technique to correct sensor drift issues in hot-wire anemometry. *Meas. Sci Technol.* **25**, 105304.

TAYLOR, G.I. 1938 The spectrum of turbulence. *Proc. R. Soc. Lond.* A **164** (919), 476–490.

THEODORSEN, T. 1952 Mechanism of turbulence. In *Proc. Midwest. Conf. Fluid Mech., 2nd, Columbus, Ohio*, pp. 1–18.

TOMKINS, C.D. & ADRIAN, R.J. 2003 Spanwise structure and scale growth in turbulent boundary layers. *J. Fluid Mech.* **490**, 37–74.

TOWNSEND, A.A. 1956 *The Structure of Turbulent Shear Flow*, 1st edn. Cambridge University Press.

WALLACE, J. 2014 Space–time correlations in turbulent flow: a review. *Theor. Appl. Mech. Lett.* **4**, 022003.

WARK, C.E. & NAGIB, H.M. 1991 Experimental investigation of coherent structures in turbulent boundary layers. *J. Fluid Mech.* **230**, 183–208.

WEI, T. & WILLMARTH, W. 1989 Reynolds number effects on the structures of a turbulent channel flow. *J. Fluid Mech.* **204**, 57–95.

WILLERT, C.E., SORIA, J., STANISLAS, M., KLINNER, J., AMILI, O., EISFELDER, M., CUVIER, C., BELLANI, G., FIORINI, T. & TALAMELLI, A. 2017 Near-wall statistics of a turbulent pipe flow at shear Reynolds numbers up to 40 000. *J. Fluid Mech.* **826**, R5.

ZAMAN, K.B.M.Q. & HUSSAIN, A.K.F. 1981 Taylor hypothesis and large-scale coherent structures. *J. Fluid Mech.* **112**, 379–396.

ZANOUN, E.-S., EGBERS, C., NAGIB, H., DURST, F., BELLANI, G. & TALAMELLI, A. 2021 Wall friction relations in wall bounded shear flows. *Eur. J. Mech. B/Fluids* **89**, 171–179.

ZANOUN, E.-S., ÖNGÜNER, E., EGBERS, C., BELLANI, G. & TALAMELLI, A. 2019 One-dimensional flow spectra and cumulative energy from two pipe facilities. In *Progress in Turbulence VIII iTi* (ed. R. Örlü, A. Talamelli, J. Peinke & M. Oberlack), vol. 226, pp. 209–214. Springer.